Università degli Studi di Pisa

Facoltà di Scienze Matematiche, Fisiche e Naturali

Corso di Laurea Specialistica in Scienze Fisiche

Anno Accademico 2007/2008

Tesi di Laurea Specialistica

Modulation of Josephson current in out-of-equilibrium superconductors

Candidato

Stefano Tirelli

Relatore

Prof. Fabio Beltram
Dr. Francesco Giazotto

To my family, in the broadest sense

Contents

Introduction

Since the liquefaction of helium by Kramerlingh Onnes in 1911 and the birth of low temperature physics, superconducting systems have brought to the attention of the scientific community a number of new and interesting physical phenomena. Recently, out-of-equilibrium superconducting systems gained much attention from both the theoretical and experimental points of view and allowed the realization of controllable Josephson junctions through injection of an electric current.

The first proposal for the use of out-of-equilibrium phenomena in superconductors was put forward by Parmenter in 1961. Early demonstrations of enhancement of superconductivity by quasiparticles extraction were performed by Chi and Clarke in 1979 and by Blamire *et al.* in 1992. More recently (1999) Manninen *et al.* demonstrated electron-cooling effects by extraction of quasiparticles in an array of Al-AlO-Ti junctions. It was also experimentally demonstrated that the Josephson current in superconductor-normal metal-superconductor (SNS) junctions can be controlled by injection of a current through the normal metal, even leading to a phase reversal of the supercurrent (π-junction).

Relevant applications of superconducting-insulator-normal metal symmetric junctions (SINIS) were demonstrated, but many aspects of all-superconducting tunnel devices (SISIS) still lack experimental investigation. Recent theoretical papers addressed all-superconducting tunnel structures for their use as controllable Josephson junctions, but an analysis of the behavior of the supercurrent in out-of-equilibrium superconductors was never performed.

It is in this framework that this work originates, with the purpose of designing and fabricating superconducting tunnel junctions controllable by extraction of quasiparticles in order to investigate the behavior of the Josephson current in out-of-equilibrium superconductors. To do this I fabricated devices consisting of a mesoscopic superconducting titanium island connected to two aluminum superconducting reservoirs through tunnel junctions. By voltage biasing of the reservoirs, quasiparticles are extracted from the island and an out-of-equilibrium distribution function

3

is induced in its electron system. As the bias voltage of the reservoirs is varied, the effect of the out-of-equilibrium distribution on the Josephson supercurrent flowing through the island and two additional aluminum tunnel contacts is studied.

In this thesis I shall present experimental data of some devices that I fabricated at NEST laboratory in Pisa and measured at low temperature at Helsinki University of Technology. The analysis of the Josephson current in steady-state out-of-equilibrium regime will identify the basic phenomenological aspects of all-superconducting structures and explore their suitability as superconducting transistors or electronic refrigerators. The data will be interpreted with the accepted quasiequilibrium theory. New phenomenological aspects will be pointed out and interpreted by extending the present theory.

This thesis is structured as follows:

Chapter 1: This chapter introduces the theoretical concepts which are the basis of the following interpretation of the data. The chapter reviews the basics of Bardeen-Cooper-Shrieffer (BCS) theory, the standard description of tunneling in normal and superconducting junctions, and the theoretical approaches to model out-of-equilibrium superconductors.

Chapter 2: Gives an overview on the state-of-the-art in the experimental study of out-of-equilibrium Josephson junctions. This chapter reviews the main experimental findings and some experimental techniques that constitute the framework in which my thesis work originated.

Chapter 3: Details the experimental techniques and the processing steps used for the fabrication of our superconducting controllable tunnel junctions. Special attention is devoted to the fabrication of tunnel junctions, one of the most crucial steps in the fabrication of the device.

Chapter 4: Shows the original experimental findings of this thesis work. The first part presents data on the out-of-equilibrium behavior of Josephson current in our structures. The second part presents the theoretical model used to interpret the data.

Chapter 1

Tunneling and nonequilibrium in superconductors

1.1 The superconducting state

While the theories of London, Pippard and especially Ginzburg and Landau [33] were able to explain some of the peculiar phenomenology of superconductivity in the early '50, it was not until the idea of binding electron in pairs by an attractive interaction, introduced by Cooper in 1956 that a satisfactory microscopic explanation of the origin of the superconductivity was presented. In the free-electron model of metals, the ground state at zero temperature is the Fermi state, with electrons populating energy levels up to the Fermi energy E_F. Cooper showed that upon introduction of a binary attractive potential, the electron gas could decrease its overall energy by coupling electrons in singlet pairs, producing a new ground state with a lower energy, the superconducting state. In this state two kinds of charge carriers coexist in the metal: conduction electrons and Cooper pairs. The latter have a charge equal to $2e$ and null total spin, and thus are not subject to the Pauli exclusion principle. The possibility of the pairs of being all coherently condensed in a single energy level produces the more apparent effects of superconductivity such as persistent currents and the perfect diamagnetic behavior.

The origin of the attractive potential between the free carriers can be explained by considering the interaction between electrons and the lattice: it is possible for an electron to emit a lattice phonon which is then immediately re-absorbed by another electron, this process can be shown [10] to generate a net attractive potential between particles with energies $|\varepsilon| < \hbar\omega_D$, where ω_D is the Debye frequency of the

lattice, $\hbar$ is the Planck constant, and ε is measured from the Fermi energy. At zero temperature, the effect of this potential is that an energy range around the Fermi energy, much smaller than $\hbar\omega_D$ for conventional superconductors, is *depleted* from electron carriers, originating what is called a *superconducting gap*, whose zero temperature value we denote as Δ_0. In the range $[\Delta_0 - E_F, E_F + \Delta_0]$ there are no single particle states available. Electrons are coupled in pairs at a single energy level equal to E_F: the only possible transitions involve breaking a pair or forming a new one.

In a superconductor, the magnitude of the energy gap influences the energy levels distribution for all the particles in the system, and it is then necessary to adopt a many-body approach. The first theory to produce a microscopic model of superconductivity with good experimental confirmation was the Bardeen-Cooper-Schrieffer (BCS) theory. In this model, rather than the individual electron and hole, we refer to the elementary excitations of the systems as *quasiparticles*, thus taking into account the fact that single particle excitations are embedded in an environment which influences their energy and their behavior. Quasiparticles are defined by their creation and destruction operators [33]

$$
\begin{aligned}
\gamma_{\mathbf{k}\uparrow}^{\dagger} &= u_{\mathbf{k}} c_{\mathbf{k}\uparrow}^{\dagger} - v_{\mathbf{k}} c_{-\mathbf{k}\downarrow} \\
\gamma_{\mathbf{k}\uparrow} &= u_{\mathbf{k}} c_{\mathbf{k}\uparrow} - v_{\mathbf{k}} c_{-\mathbf{k}\downarrow}^{\dagger},
\end{aligned}
\tag{1.1}
$$

where $\mathbf{k}$ and $\uparrow$ / $\downarrow$ represent momentum and spin of the particle, $c_{\mathbf{k}}^{\dagger}$ and $c_{\mathbf{k}}$ are the standard electron and hole creation operators, and $u_{\mathbf{k}}$ and $v_{\mathbf{k}}$ are coefficients (coherence factors) varying between -1 and 1 used to define the BCS ground state function: in a normal metal at zero temperature $v_{\mathbf{k}}^2$ is 1 up to the Fermi energy E_F and zero above it, whereas $u_{\mathbf{k}}^2$ is zero up to E_F and 1 above it. From the definitions (1.1) we can see that quasiparticles behavior changes from hole-like, electron-like or a mix of the two according to the values of $u_{\mathbf{k}}$ and $v_{\mathbf{k}}$ multiplying the electron/hole creation operators. Quasiparticle excitation energies ($E_{\mathbf{k}}$) depend from both single particle energies $\varepsilon_{\mathbf{k}}$ and the superconducting gap Δ (here supposed independent from $\mathbf{k}$), the BCS theory states $E_{\mathbf{k}} = \sqrt{\varepsilon_{\mathbf{k}}^2 - \Delta^2}$. From this we can calculate their density of states D_S^*. From the one-to-one correspondence between single particle excitations and quasiparticles, we can write $D_S^*(\varepsilon)d\varepsilon = D_N(E)dE$, where $D_N(E)$ is

the normal-metal density of states, so we have

$$D_S(E) = \frac{D_S^*(\varepsilon)}{D_N(E)} = \frac{dE_{\mathbf{k}}}{d\varepsilon_{\mathbf{k}}} = \begin{cases} \frac{\varepsilon_{\mathbf{k}}}{\sqrt{\varepsilon_{\mathbf{k}}^2 + \Delta^2}} & \text{if } |\varepsilon_{\mathbf{k}}| > \Delta_0 \\ 0 & \text{if } |\varepsilon_{\mathbf{k}}| < \Delta_0 \end{cases},$$

where we used D_S^* for the absolute, unnormalized density of states and D_S for the normalized quantity. The quasiparticle density of states is zero inside the gap and presents divergencies for $E \to (E_0 - \Delta_0)^-$ and $E \to (E_0 + \Delta_0)^+$. This means that there is a huge number of states available in the energy region next to the superconducting gap edge, this remarkable feature shows up clearly in tunnel junctions current-voltage characteristics and finds application in devices where a high tunneling probability is desired (see following section). In a superconducting ground state at zero temperature, the quasiparticle states are fully occupied up to $E_F - \Delta$ and unoccupied from $E_F + \Delta$, while for higher temperatures an increasingly high number of quasiparticles is excited, and less and less pairs are able to participate in the condensate. This in turn reduces the gap magnitude, freeing even more states for transitions and reducing the minimum energy needed for breaking a Cooper pair. Because of this self-enhancing process, the gap behavior versus temperature must be calculated self-consistently through the BCS equation for the superconducting gap:

$$1 = U_0 D_N(E_F) \int_{-\hbar\omega_D}^{\hbar\omega_D} \frac{d\varepsilon}{\sqrt{\varepsilon^2 + \Delta^2}} \tanh\left(\frac{\sqrt{\varepsilon^2 + \Delta^2}}{2k_B T}\right), \tag{1.2}$$

where k_B is the Boltzmann constant, T is temperature and the integration is performed over an energy shell $\hbar\omega_D$ equal to the Debye energy of the lattice; in the *average potential approximation* the phonon-mediated electron-electron attractive potential is considered constant and equal to U_0 in this range and null elsewhere; moreover the density of states is also considered constant in this range ($\hbar\omega_D \ll E_F$) and approximated with its value at the Fermi energy, carrying the term out of the integral. In Fig. 1.1 a numerical calculation of this relation is shown: the gap is nearly constant up to about $T \approx 0.4T_c$, then suddenly drops to zero at the critical temperature T_c. This relation is valid for conventional superconductors where the average potential approximation holds. In the weak coupling limit $U_0 D_N(E_F) \ll 1$ and $\hbar\omega_D/k_B T_c \ll 1$, the zero temperature gap Δ_0 and the critical temperature T_c are linked by the equation

$$\Delta_0 = 1.764 k_B T_c, \tag{1.3}$$

which is one of the most experimentally established results of the BCS theory.
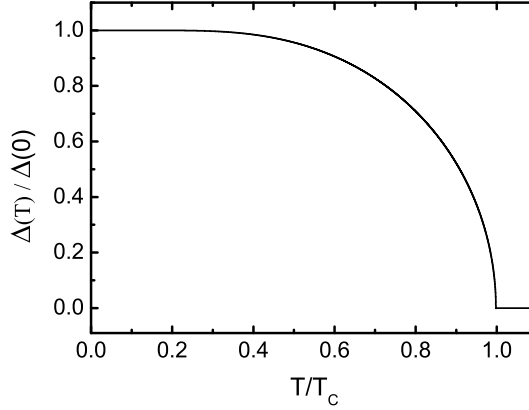
Figure 1.1: Normalized energy gap versus reduced temperature T/T_c, numerically calculated from equation (1.2).

1.2 Tunneling in superconductors

The key transport process that allows realization of controllable solid-state nano-junctions is electron tunneling. In this section we shall review the basic treatment of this process in normal and superconducting systems. A junction made by two metals separated by a thin insulating layer may allow charge carriers to tunnel through the barrier with a non vanishing probability. For the probability to be finite, electrons must find a free state at the energy level in the target metal matching the originating metal. This is determined by the electron distribution functions and by the number of energy levels available in that range, i.e., the density of states. In the case of a junction made of two identical, normal metals at zero temperature, all electron bands up to their Fermi energy are full, and no tunneling is possible unless we apply a voltage bias V between the two (see Fig. 1.2a). The band structure of the negatively biased metal "shifts" up with respect to the other and electrons in the uppermost bands are able to tunnel into the free states above the Fermi energy of the positively biased metal. By increasing the bias voltage more and more states are available for tunneling, and the tunneling current increases accordingly. The current flowing in such a system can be calculated approximating the transition process with a perturbation represented by the so called tunneling Hamiltonian

$$H_t = \sum_{\mathbf{k}_l \mathbf{k}_r} \mathcal{T}_{\mathbf{k}_l \mathbf{k}_r} c_{\mathbf{k}_r}^\dagger c_{\mathbf{k}_l} + \sum_{\mathbf{k}_l \mathbf{k}_r} \mathcal{T}_{\mathbf{k}_r \mathbf{k}_l} c_{\mathbf{k}_l}^\dagger c_{\mathbf{k}_r}, \tag{1.4}$$
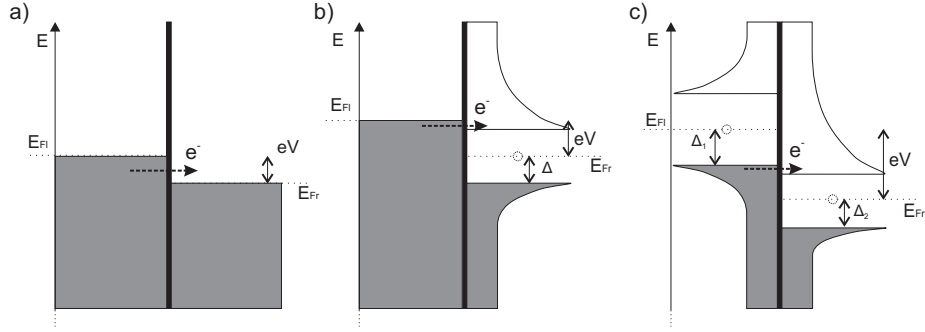
Figure 1.2: Tunneling graphs in the semiconductor model at $T = 0$ for the cases of (a) NIN, (b) NIS, (c) S_1IS_2 junctions. In the graphs the thick black vertical lines represent the insulating barriers, energies are represented on the vertical axis and the density of states is represented on the horizontal axis, showing the divergencies in the superconductors at $E_F \pm \Delta$. The grey regions represent occupied energy levels, while inside the superconducting gap for $E_F - \Delta < E < E_F + \Delta$ there are no available states.

where the subscripts l,r refer respectively to the left metal and the right metal, and $\mathcal{T}_{\mathbf{k_l k_r}}$ is a coefficient depending on the features of the insulating barrier. This coefficient is, in general, function of $\mathbf{k_l}$ and $\mathbf{k_r}$. If the barrier is sufficiently thin to exclude any interaction within it, and produces a high enough voltage step, it can be approximated by a constant so that we can always bring it out from the sums and the integrals over $\mathbf{k}$. Using the tunneling Hamiltonian and the Fermi golden rule, we can calculate the current flowing in a normal-insulator-normal (NIN) tunneling junction with an applied voltage bias V: usually $V \ll E_F$ (measuring E_F from the bottom of the conduction band) so that we can safely assume the density of states as constant and approximate it with its value at the Fermi energy $D_N(0)$. The resulting expression for the current is:

$$I(V) = \frac{2e\pi}{\hbar}|\mathcal{T}|^2 D_{N_r}(0) D_{N_l}(0) \int_{-\infty}^{\infty} [f(E) - f(E + eV)]dE, \tag{1.5}$$

where e is the electron charge and we have shifted the zero of the potential so that it coincides with the right metal Fermi energy: $E_{F_r} = 0$ and $E_{F_l} = -eV$. Carrying out the integration on small voltage bias, the NIN case gives the simple ohmic relation

$$V = IR_N \qquad R_N = \frac{1}{G_N} = \frac{\hbar}{2\pi e^2 |\mathcal{T}|^2 D_l(0) D_r(0)}, \tag{1.6}$$

where R_N is the normal-state resistance of the junction. NIN tunneling experiments are also used to assess the quality of tunnel barriers even in superconducting junctions, by measuring the conductance above the critical temperature. The behavior of the normal-state resistance R_N can tell if the main conduction process through the barrier is electron tunneling or conventional conduction. A reliable and used experimental criteria to assess it is an increase of R_N while cooling the sample from room temperature to 4.2 K, as opposed to a decrease which happens when the resistivity is of ohmic nature, and the parabolic behavour of dI/dV for high voltage bias (see Sec. 3.1.2). These tests can be a preliminary check of the *quality* of the barrier, namely its transparency and absence of defects in the insulating layer (pinholes), that can provide unwanted conductive channels [19].

The phenomenology is quite different if one of the two metals is a superconductor. In that case we must take into account that indirect electron-electron interaction creates an energy gap where no single particle states are available for tunneling. Cooper pair tunneling from the superconductor into the normal metal is also not possible, as pairs cannot exist in the normal metal (we exclude any proximity effect by considering an ideal insulating barrier). Therefore in a NIS junction at zero temperature at the equilibrium (see Fig. 1.2(b), no tunneling is possible until a voltage bias $V > \Delta/e$ is reached. To calculate NIS tunneling current, we follow the same procedure as the NIN case, applying the Fermi golden rule with the tunneling Hamiltonian (1.4) as a perturbation, but now we must take into account that single particle excitations in the superconductor are quasiparticles described by the operators (1.1) and their density of states cannot be approximated with a constant value because of its singularity. Performing the necessary substitutions we obtain

$$
\begin{aligned}
I^{NIS}(V) &= \frac{1}{R_N e} \int_{-\infty}^{\infty} \frac{D_S^*(E)}{D_N(0)} [f(E) - f(E + eV)] dE \\
&= \frac{1}{R_N e} \int_{-\infty}^{\infty} \frac{|E|}{\sqrt{E^2 + \Delta^2}} [f(E) - f(E + eV)] dE,
\end{aligned}
\tag{1.7}
$$

where we have used (1.1) for the density of states. The current [see plot in Fig. 1.3(a)] has a sharp onset at $eV = \Delta$, where electrons coming from the normal side find a large number of available states to tunnel to. At finite temperatures, this onset is rounded by the presence of thermally excited quasiparticles which allow conduction before $eV = \Delta$.

When both metals of the junction are superconducting (i.e., S_1IS_2) the current-voltage characteristics resemble that of a NIS junction at $T = 0$, but the presence
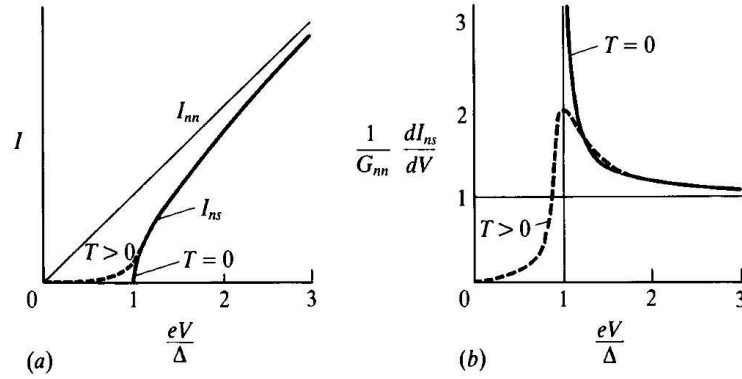
Figure 1.3: Plots of current-voltage characteristics and differential conductance of a NIS junction at $T = 0$ and $T \neq 0$. Panel (a) shows the I-V of a NIS junction, the onset at $eV/\Delta = 1$ is rounded by the presence of thermally excited quasiparticles at $T \neq 0$, and tends asymptotically to the constant slope I_{nn} of the normal state NIN (normalized so that $(dI/dV)_{NIN} = 1$). Panel (b) shows the differential conductance $G_{NIS}(V)$, the effect of thermal excitation is to remove the discontinuity at $eV = \Delta$ turning it into a peak. For $V \to +\infty$ G_{NIS} tends to the NIN value; also note the finite conductance for $eV/\Delta < 1$ at $T > 0$ as opposed to the vanishing value for $T \to 0$. Adapted from [33].

of two different gaps does not allow quasiparticle tunneling up to a bias voltage equal to the sum of the two, $eV = \Delta_1 + \Delta_2$ (2Δ in case of equal gaps). Two density of states discontinuities enhance tunneling at this voltage, making the onset more abrupt than the NIS case. For $T \neq 0$ the I-V is different whether the two superconducting metals have equal of different energy gaps: when one gap is smaller than the other, there is a finite bias voltage $eV = \Delta_1 - \Delta_2$ for which the discontinuities in the density of states at $E_F + \Delta_1$ and $E_F + \Delta_2$ match at the same energy level: at temperature higher than zero these energies are partially occupied by thermally excited quasiparticles which find a large number of available state to tunnel to, producing a logarithmic singularity in the I-V's. By increasing temperature more quasiparticles are excited, making the singularity more pronounced, while the BCS dependence of the gaps make it shift toward smaller bias voltages. When the gaps are identical (i.e., SIS case) the singularity would be at $V = 0$ regardless of temperature, but quasiparticle current at zero bias is vanishing so the effect is that we get an infinite slope of the I-V at $V = 0$. In the S_1IS_2 case, the quasiparticle current can be found in the same way as the other cases. Introducing the superconducting density of states of the two metals the expression obtained is thus

11
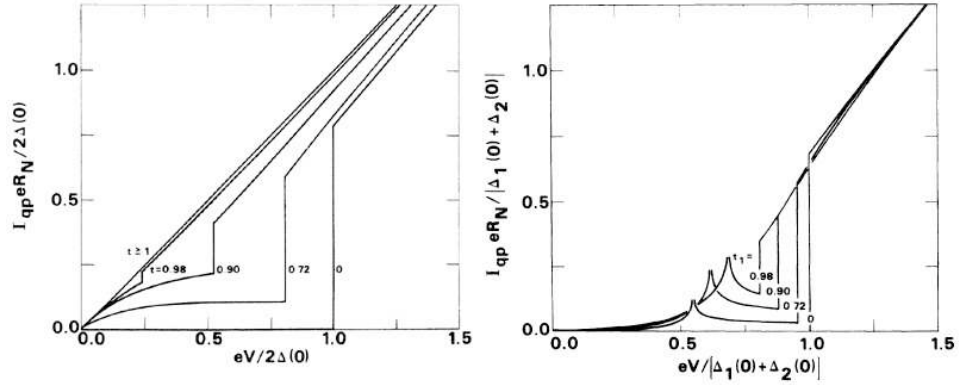
Figure 1.4: Plots of a SIS (left) and S_1IS_2 (right) quasiparticle currents at different temperatures $t = T/T_{c1}$, where T_{c1} is the critical temperature of the first superconductor. In the SIS case (left) at $T = 0$ no current flows until a sharp onset at $eV = 2\Delta$ occurs, then it asymptotically tends to the ohmic characteristic $V = R_N I$, where R_N is the normal-state resistance. At $T > 0$ for $V \rightarrow 0$ the current vanishes with infinite slope though this is not evident from the scale of the graph. In the S_1IS_2 case (right) at $T \neq 0$ a logarithmic singularity appears at $eV = \Delta_2 - \Delta_1$. Note the increase in magnitude of this singularity and shift in energy as temperature is increased. Adapted from [15].

$$I^{SIS}(V) = \frac{1}{R_N e} \int_{-\infty}^{\infty} \frac{|E|}{\sqrt{E^2 + \Delta_1^2}} \frac{|E + eV|}{\sqrt{(E + eV)^2 + \Delta_2^2}} [f(E) - f(E + eV)]dE. \quad (1.8)$$

A direct experimental measurement of $D_S(E)$ is conveniently performed through the differential conductance dI/dV, obtained differentiating equation (1.7):

$$G_{NIS}(V) = \frac{dI^{NIS}}{dV} = -\frac{1}{R_N} \int_{-\infty}^{\infty} D_S(E) \left[\frac{\partial f(E + eV)}{\partial(eV)} \right] dE.$$

The function $\frac{\partial f(E+eV)}{\partial(eV)}$ is sharply peaked at $E = -eV$ (we choose $E_F = 0$) and tends to a δ-function for $T \rightarrow 0$. In this limit the differential conductance becomes directly proportional to the density of states: $G_{NIS} = D_S(e|V|)/R_N$. Figure 1.3(b) shows the differential conductance G_{NIS} versus voltage, for $T = 0$. Also in this case the conductance is a direct representation of the density of states, while for $T > 0$ thermally excited quasiparticles cause a finite conductivity even for $eV < \Delta$, and the discontinuity at $V = \Delta/e$ is smeared into a peak.

From the I-V characteristics we can obtain information about the quality of the insulating barrier and the purity of the superconducting metal. Non-ideal barriers may allow conduction within the gap caused by processes like Andreev reflection (see [33]) at the interface due to pinholes in the insulator. Also, impurities in the

12
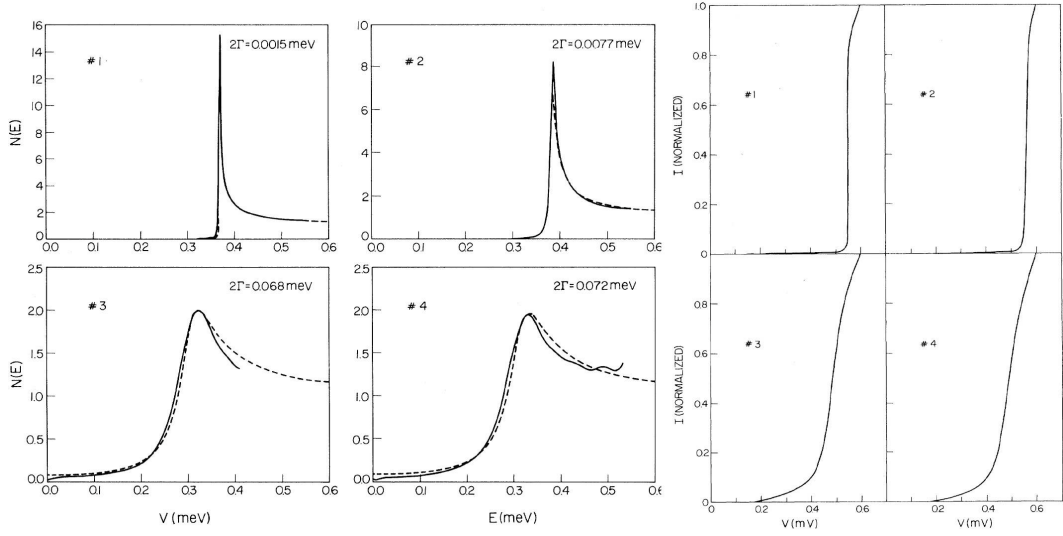
Figure 1.5: Plots of the calculated smeared density of states (1.9) (dashed lines) and experimental data (solid lines) for S_1IS_2 Al-oxide-granular Al junctions. Granular Al has a slightly smaller gap than Al, and in samples from 1 to 4 showed an increasing resistivity. This is modeled by a γ parameter ranging from about $4 \cdot 10^{-3}\Delta_{Al}$ to $2 \cdot 10^{-1}\Delta_{Al}$ (labeled here as Γ). This leads to a rounding of the sharp features appearing in the differential conductance (left panels) and I-V (right panels). Adapted from [8].

superconductor can create sub-gap states supporting single particle conduction within the otherwise forbidden energy range $E_F - \Delta < E < E_F + \Delta$. To take into account for this non ideality, it is common to introduce a phenomenological parameter γ which adds an imaginary part to the energy in the density of states with the effect of *smearing* its divergencies at $E_F \pm \Delta$. The smeared density of states thus becomes:

$$D_S(E,\gamma) = \left| \mathrm{Re}\left[\frac{E + i\gamma}{\sqrt{(E + i\gamma)^2 + \Delta^2}} \right] \right|. \tag{1.9}$$

Typical values for γ in barriers with very small sub-gap leakage are in the range $10^{-6} - 10^{-4}\Delta$. For big enough γ at low temperature it is possible to observe a small but finite conductivity for all bias voltages within the gap: at low voltages, the differential resistance is determined by γ so that $R_{NIS}(0) \approx R_{NIS}(\infty)\Delta/\gamma$, and a frequently used way to estimate it is based on the low temperature ratio $R_{NIS}(\infty)/R_{NIS}(0) = \gamma/\Delta$. The effect of a finite γ on conductance and I-V characteristics is shown in Fig. 1.5 for Al-oxide-Al granular junctions (S_1IS_2) where γ is changed by using samples with different resistivities of granular Al: upon increasing
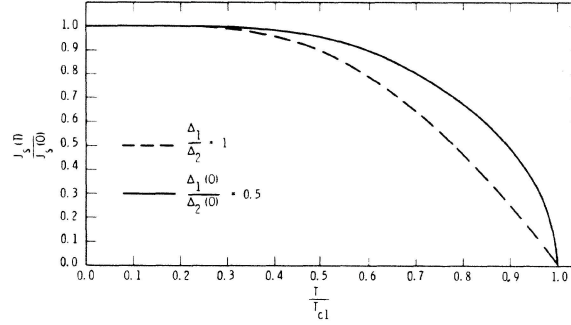
Figure 1.6: Plots of the critical current versus temperature in the case of a SIS junction (solid line) and a S_1IS_2 junction with $2\Delta_1(0) = \Delta_2(0)$. Scales are normalized to the zero temperature value of the critical current ($J_S(0)$ in the plot) and the first superconductor critical temperature T_{c1}. Adapted from [1].

γ the sharp features appearing at $eV = \Delta_1 + \Delta_2$ in the I-V become smeared, while the conductivity within the gap increases.

1.2.1 Pair tunneling

Cooper pairs can also tunnel through thin insulating barriers, producing non dissipative currents even in tunnel junctions. A superconducting junction can sustain a finite current of maximum magnitude I_c (DC Josephson effect), which depends on the phase difference between the order parameter of the two superconductors. If a voltage is applied to the junction, the phase difference $\delta\phi$ evolves linearly as $d(\delta\phi)/dt = 2eV/\hbar$, producing an alternating current (AC Josephson effect). In this case there is a difference of eV between the Cooper pairs energy levels of the two superconductors forming the junction, this produces emission of electromagnetic radiation (Josephson radiation) of frequency $\nu = 2eV/\hbar$ associated with pair tunneling.

An analytical espression for the DC critical current I_c was given by Ambegaokar and Baratoff [1]. For different superconductors

$$I_c = \frac{2}{eR_N} \frac{\Delta_1\Delta_2}{\Delta_1 + \Delta_2} K\left(\frac{|\Delta_1 - \Delta_2|}{\Delta_1 + \Delta_2}\right), \tag{1.10}$$

where K is the complete elliptical integral of the first kind. The magnitude of the current is inversely proportional to the normal-junction state resistance R_N, and depends nonlinearly on the gap values $\Delta_{1,2}$ of the two superconductors. Its behavior as a function of temperature for identical superconductors is somewhat similar to

the BCS gap (see Fig. 1.6), and the study of the DC Josephson current can be used to estimate the superconducting gaps magnitudes and their critical temperatures. Because of its phase dependence, DC Josephson current is extremely sensitive to electromagnetic fields, and demands particular attention to filtering noise in the equipment used to detect it.

1.3   Out-of-equilibrium superconductivity

When a metallic system is in thermal equilibrium, its electronic energy bands are occupied according to the Fermi-Dirac distribution

$$f_0(E) = \frac{1}{1 + e^{\left(\frac{E - E_F}{k_B T}\right)}}, \tag{1.11}$$

where E is the energy of the electron state, and E_F is the Fermi energy. The parameter T defines the thermodynamic temperature in a system at equilibrium. A metallic film can be thought to be made of two interacting thermodynamic systems: the electron gas and the underlying ion lattice. At the equilibrium, both systems are characterized by the same thermodynamic temperature T. Under certain conditions, however, the electronic distribution may be characterized by a different temperature T_e or even a different distribution function altogether, which may even not define a thermodynamic temperature. In these cases the system is said to be *out of equilibrium*. In this section we shall analyze how these conditions can be achieved, how this reflect on the observable properties of a superconductor, and this phenomenology has been analyzed by the models existing in the literature.

When they are not subjected to external excitations, electrons in a metallic system tend in time to assume the distribution function (1.11), therefore an out-of-equilibrium steady state can be realized only by means of some external action which modifies the population of the electronic levels. The internal processes that tend to restore the equilibrium distribution function are inelastic scattering events, so to achieve a steady state deviation from the equilibrium than the relaxation processes, i.e., the number of particles that relax towards equilibrium in the unit time must be smaller than the ones that are excited or extracted by the external perturbation. If we disregard the individual scattering process we can suppose that the distribution function relaxes to the equilibrium value with an exponential law with characteristic time τ_R. In the *relaxation time approximation* the evolution of the

distribution function (f) is written as:

$$\left(\frac{\partial f}{\partial t}\right) = -\frac{f(E) - f_0(E)}{\tau_R}.$$

The electrons of the Fermi sea may undergo collisions with impurities, with phonons, or with other electrons. The relevance of each of these interactions in a system can be preliminarily assessed by comparing their characteristic scattering length (i.e., mean free path between interaction of that kind) with the size of the system. For example, in a mesoscopic quasi-1D wire relaxation can be limited by making the wire length smaller than the characteristic length of inelastic scattering processes. In such case it is possible to induce a steady-state out-of-equilibrium distribution inside the wire. Only inelastic scattering processes contribute to relaxation of the distribution function toward equilibrium, i.e. electron electron (e-e), electron-phonon interaction (e-ph) or scattering with magnetic impurities. Their low-temperature scattering lengths are typically $l_{e-e} \approx 1 \dots 10\mu$m for electron-electron scattering and $l_{e-ph} \approx 20\mu$m for election-phonon scattering at 1 K.

In the case of a mesoscopic wire of length $L \ll l_{e-e} \ll l_{e-p}$, relaxation toward equilibrium is strongly suppressed, the electronic distribution may attain very peculiar profiles and (1.11) no longer describes the distribution in the system. This is the *nonequilibrium* limit. In this regime it is not possible to define temperature as a parameter of the Fermi-Dirac distribution, but it is sometimes useful to define an effective temperature T^* through an observable quantity such as the superconducting gap. In the weak coupling approximation, with the notation used in Section 1.1 the BCS gap equation (1.2) can be written to explicitly depend on the distribution function

$$1 = U_0 D_N(E_F) \int_{-\hbar\omega_D}^{\hbar\omega_D} \frac{d\varepsilon}{\sqrt{\varepsilon^2 + \Delta^2}} [1 - 2f(\varepsilon)], \tag{1.12}$$

which must be used self consistently to determine Δ for any distribution function $f(E)$. In the case of a thermal distribution $f_0(T)$ we find the standard BCS dependence of $\Delta(T)$ shown in Fig. 1.1. In the case of a nonequilibrium distribution f_{neq}, we can define an effective temperature T^* so that $\Delta[f_0(T^*)] = \Delta[f_{neq}(E)]$ where $\Delta[f_{neq}(E)]$ is the gap value from (1.12) self-consistently using f_{neq}. This is not the only possible definition for an effective temperature, therefore T^* has to be regarded merely as a descriptive parameter whose definition is not unambiguous.

If the characterstic size L of the system is so that inelastic electron-electron scattering is not negligible but electron-phonon interaction is, i.e., $l_{e-e} \ll L \ll l_{e-ph}$, electrons attain a Fermi-Dirac distribution characterized by a well defined electronic

temperature T_e. However, the lattice phonon temperature T_{ph} can be different from the electronic one T_e. Electron-phonon scattering is strongly temperature-dependent: at 100 mK, for example, we have $l_{e-ph} \approx 670\mu$m. In mesoscopic devices, the electron system can be thus treated as a system at equilibrium with temperature T_e which weakly interacts with its lattice phonons system with a small but finite thermal conductance. This is called *quasiequilibrium* limit.

In the next sections we shall review some theoretical treatments introduced to model $S_1IS_2IS_1$ and SINIS devices in nonequilibrium and quasiequilibrium regimes.

1.3.1 Nonequilibrium regime

In the nonequilibrium regime energy-relaxation processes are negligible. The electronic distribution can attain very peculiar shapes and strongly differ from the Fermi-Dirac distribution. The distribution function can be computed for the case of a complete absence of scattering processes or introducing some inelastic relaxation in the equations. For both cases, two approaches were presented in the literature, one by Laakso *et al.* [20] who used a detailed microscopic kinetic theory in the quasiclassical Keldysh Green function formalism, and another by Heslinga *et al.* [16] who described the interactions within the system by a relaxation-time approximation. We shall review the study of a $S_1IS_2IS_1$ system within the latter framework and present some results from the microscopic analysis.

In a $S_1IS_2IS_1$ junction, the volume to be driven out of equilibrium is the central superconducting island S_2. The modification of the distribution function inside it is achieved by applying a voltage bias to the superconducting reservoirs S_1 to which the island is in contact through tunnel junctions. Quasiparticles are extracted from the island to the superconducting leads, and electronic occupations modified. The model developed by Heslinga *et al.* [16], determines the occupation of the electronic levels in the metallic island (S_2) by considering a particle number conservation equation for each energy level. If energy-relaxation scattering processes are absent, each level of energy E inside the island S_2 can be populated or depopulated only by extraction or injection from the superconducting leads (S_1). In practical cases energy relaxation processes cannot be completely neglected, and to take them into account one can introduce a (de)population rate of each energy level through the relaxation time approximation. The relaxation time approximation disregards the nature of each scattering process by introducing a single characteristic relaxation time τ_R with which the distribution function relaxes to equilibrium value f_0. The number of electrons that relax per unit time at a given energy can

thus be expressed as

$$\delta N(E) = \mathcal{V} D^*(E) \frac{f_2(E) - f_0(E)}{\tau_R}, \tag{1.13}$$

where $\mathcal{V}$ is the volume of the island (S$_2$), D^* is the unnormalized density of states at the given energy, $f_0(E)$ is the equilibrium distribution (1.11) and $f_2(E)$ is the actual distribution function of the island. Other than through a scattering process, an electron can leave (or enter) an energy level when it is extracted (or injected) by the reservoir (S$_1$) of the S$_1$IS$_2$IS$_1$ device. The charge that flows in the unit time from the central island to a reservoir is expressed by the SIS current [Eq. 1.8], The number of particles extracted from each energy level per unit time can thus be expressed by the integrand divided by e. When the reservoirs are biased with a voltage V_c, after labeling $E^+ = E + eV_c/2$ and $E^- = E - eV_c/2$ one obtains the particle flux to the left and right reservoirs (labeled $1l$ and $1r$):

$$\delta N_{2 \to 1l}(V_c) = \tfrac{1}{R_N e^2} D_1(E^-) D_2(E) [f_2(E) - f_0(E^-)] \tag{1.14}$$

$$\delta N_{2 \to 1r}(V_c) = \tfrac{1}{R_N e^2} D_1(E^+) D_2(E) [f_2(E) - f_0(E^+)]. \tag{1.15}$$

In a steady-state out-of-equilibrium condition, the number of particles relaxing through scattering processes must be equal to the number of particles injected and extracted by the reservoirs, so one must impose $(1.13) = (1.15) + (1.14)$. From this expression one can determine the nonequilibrium distribution $f_2(E)$:

$$f_2(E) = \frac{D_1(E^-) f_0(E^-, T_1) + D_1(E^+) f_0(E^+, T_1) + \frac{f_0(E)}{\Gamma \tau_R}}{D_1(E^-) + D_1(E^+) + \frac{1}{\Gamma \tau_R}}, \tag{1.16}$$

where

$$\Gamma = \frac{1}{D_2^*(E_F) \mathcal{V} R_N e^2}, \tag{1.17}$$

so that $\Gamma \tau_R$ can be seen as a relaxation time normalized to the injection rate and the states available at the Fermi energy of the island. To achieve nonequilibrium, the injection rate must be larger than the relaxation rate, i.e., $\Gamma \tau_R \gg 1$. If $\Gamma \tau_R \ll 1$ scattering processes are too fast, and f_2 tends to the equilibrium distribution f_0. A small volume of the island $\mathcal{V}$, as well as small normal-state resistance R_N of the tunnel junctions are needed to realize full nonequilibrium. Note that f_2 does not depend on the density of states $N_2(E)$ of the island [9]. This formula is thus valid for both the cases in which the island is either normal (SINIS) or superconducting (S$_1$IS$_2$IS$_1$).
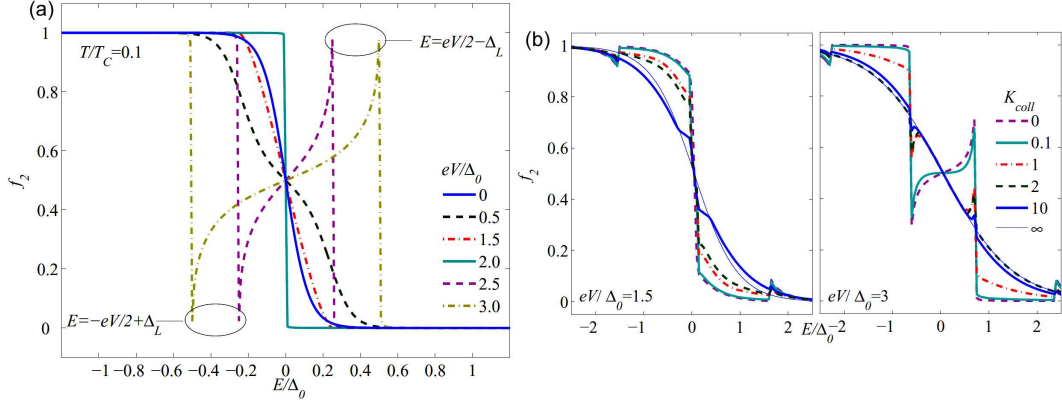
Figure 1.7: Panel (a): Distribution function of the central island in the absence of relaxation for different injection voltages at $T = 0.1T_{c1}$. It is assumed $\Delta_L = \Delta_0$ as the gap value in the superconducting leads (Δ_1 in the notation used in the text). (b) Distribution function for $eV = 1.5\Delta_1$(left) and $eV = 3\Delta_1$(right) in nonequilibrium with non-zero relaxation. Relaxation strength is indicated by the factor $\mathcal{K}_{coll}$. The limit $\mathcal{K}_{coll} = \infty$ reduces to quasiequilibrium. Adapted from [20].

Figure 1.7(a) shows the distribution function in absence of relaxation ($1/\Gamma\tau_R = 0$) versus injection voltage V_c, at $T = 0.1T_c$, where T_c is the critical temperature of leads and a finite smearing parameter $\gamma = 10^{-4}\Delta_1$ is used in both D_1 and D_2 in (1.16). At low injection voltages [$eV_c = 0.5\Delta_1$ and $eV_c = 1.5\Delta_1$ in Fig. 1.7(a)] the island is heated up and the distribution function attains a more rounded profile. This is caused by the assumption of a non-zero sub-gap conductance ($\gamma \neq 0$), which constitute a dissipative channel that generates heat. This anomalous heating is absent if $\gamma = 0$. As soon as $eV_c = 2\Delta_1$ the reservoir bands are in the optimal configuration for maximizing the extraction of hot quasiparticles by tunneling, and the maximum cooling power is achieved. This compensates the heating from sub-gap dissipative channels and realizes a perfectly sharp, zero temperature-like distribution function [solid cyan line in Fig. 1.7(a)]. At higher injection voltages, hot quasiparticles are injected in the central island and the distribution function departs strongly from equilibrium attaining an inverted profile [yellow and purple dashed lines in Fig. 1.7(a)]. If some inelastic relaxation is present [i.e., $1/\Gamma\tau_R \neq 0$ in (1.16)] the sharp features of the nonequilibrium distribution function are progressively smeared up to the point where we retrieve the equilibrium distribution function for the electrons. Figure 1.7(b) shows the results of a nonequilibrium distribution function in presence of nonvanishing relaxation calculated by means of the microscopic kinetic theory [20], instead of the relaxation-time approximation. Relaxation strength is represented by
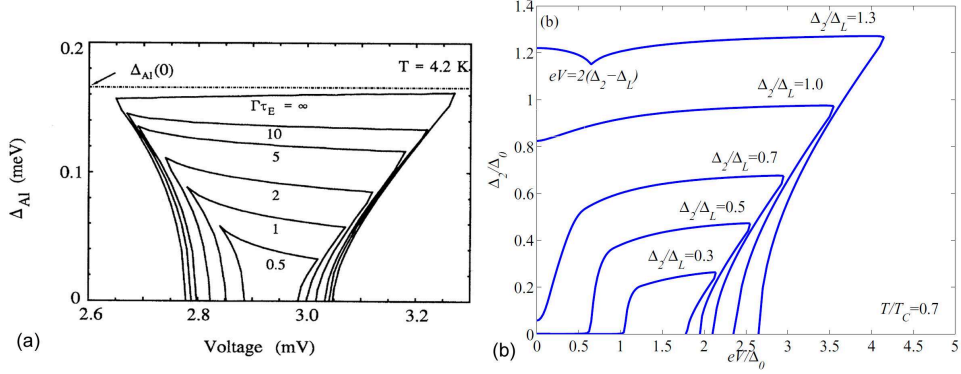
Figure 1.8: Panel (a): Calculated Al gap data versus injection in an Nb-Al-Nb $S_1IS_2IS_1$ system at 4.2 K, for different relaxation strength. Full nonequilibrium is the case of $\Gamma\tau_R = \infty$. Note the multi-valuedness of Δ_{Al} (adapted from [16]). Panel (b): Superconducting gap value versus injection for a $S_1IS_2IS_1$ system in full nonequilibrium with different ratios between the island gap Δ_2 and the leads Δ_L (Δ_1 in the notation used in the text), at $T = 0.7T_c$ where T_c is the leads critical temperature (adapted from [20]).

the constant $\mathcal{K}_{coll}$ instead of $\Gamma\tau_R$.

Once the nonequilibrium distribution function is known, one can calculate all the other physical properties of the system. Figure 1.8(a) shows the superconducting gap versus injection voltage for a niobium-aluminum $S_1IS_2IS_1$ system at $T = 4.2$ K self-consistently calculated from the BCS gap equation (1.12). The critical temperature of aluminum is 1.2 K, so that at 4.2 K the gap at equilibrium is zero. However for $eV_c = 2\Delta_1$, which corresponds to the optimal "cooling" bias, the gap is regenerated almost to its zero temperature value. By increasing inelastic relaxation the distribution function becomes more smeared (this corresponds to a higher effective temperature for the island), and the maximum gap value obtainable drops to zero accordingly. Fig 1.8(b) shows gap values for different ratios between the zero temperature gap of the island and the leads. In particular the case $\Delta_2/\Delta_1 = 0.3$ corresponds to the titanium-aluminum system studied in this thesis. Note that at the right edge of injection range where the gap is different than zero, there is always a range where the gap is multi-valued. In these bias voltage ranges the system may lie into a normal state or one of the two finite gap states. The system may jump to one state or the other giving rise to hysteretic behavior.

M.Laakso *et al.* [20], studied the behavior of the Josephson current in a cross-shaped $S_1IS_2IS_1$ device where the additional S_1 contact are used to measure Josephson current through the central S_2 island. One of the $S_1IS_2IS_1$ lines is used
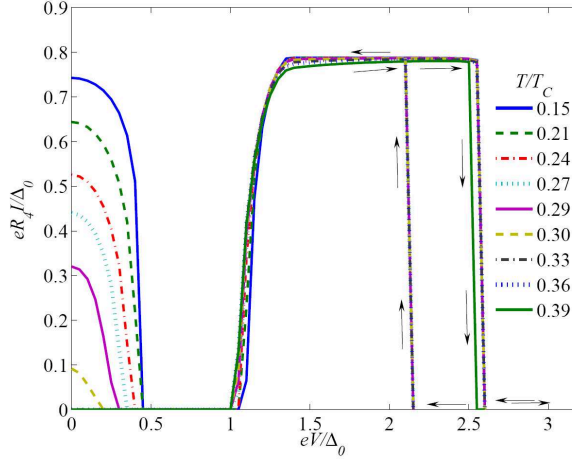
Figure 1.9: Maximum Josephson supercurrent through the additional $S_1IS_2IS_1$ probing line for $\Delta_2/\Delta_L = 0.3$, and in absence of relaxation for different temperature ratios T/T_c where T_c is the leads (S_1) critical temperature. Adapted from [20].

to drive the shared S_2 island out of equilibrium, while the supercurrent that the other $S_1IS_2IS_1$ line can sustain is monitored. For each injection voltage, the critical current can be calculated by the generalization of the Ambegaokar-Baratoff expression (1.10) for the critical current:

$$I_J = -\frac{\sin\phi}{2eR_J} \int_{-\infty}^{\infty} dE[\mathbf{f}_2(E) \cdot \mathsf{Re}\mathcal{F}_2(E) \cdot \mathsf{Im}\mathcal{F}_J(E) + \mathbf{f}_J(E) \cdot \mathsf{Re}\mathcal{F}_J(E) \cdot \mathsf{Im}\mathcal{F}_2(E)],$$
(1.18)

where $\mathbf{f}_{2,J}(E) = \tanh(E/2k_BT_{e,bath})$, $\mathcal{F}_{2,J}(E) = \Delta_{2,J}/\sqrt{(E+i\gamma)^2 - \Delta_{2,J}^2}$ and ϕ is the phase difference between superconductors. Fig. 1.9 shows the calculated supercurrent for $\Delta_2/\Delta_1 = 0.3$, at different temperatures. If temperature is lower than the critical temperature of the island T_{c2} ($T/T_c < 0.3$ in Fig. 1.9), the zero injection supercurrent is finite. At small bias voltages it get suppressed by the dissipation induced by a finite sub-gap conductance ($\gamma \neq 0$ in the density of states). As the voltage for optimal cooling $eV_c = 2\Delta_1$ is approached, the current is regenerated to its zero temperature value. This holds for all temperatures even when $T > T_{c2}$. At larger injection voltages the superconducting island S_2 is driven into the normal state ($\Delta_2 = 0$) and supercurrent drops to zero. Sweeping back the voltage, the systems stays into its zero gap state in the voltage range where the gap is multi-valued, until a fluctuation makes it jump to the superconducting state. This translates into an hysteretic behavior of the critical current versus injection voltage: this is a peculiar feature that arises in the nonequilibrium regime.

21

1.3.2   Quasiequilibrium regime

The quasiequilibrium limit corresponds to the situation in which the electron-electron interaction is efficient enough to thermalize electrons, but electron-phonon relaxation is not fast enough to thermalize their temperature to that of the lattice. In terms of characteristic lengths, this is verified when the dimensions of the metallic volume to be driven out of equilibrium are so that $l_{e-e} \ll L \ll l_{e-p}$. In this regime the electron distribution of the metal can be considered thermal (Eq. 1.11) with an electronic temperature T_e different from the lattice phonon temperature T_{ph}. The electron gas can be thus treated as a thermodynamic system in equilibrium, weakly coupled to the lattice phonons and its temperature can be determined with a heat balance equation, which takes into account all the mechanisms driving power into the system [see Fig. 1.10(a)].

In order to write the heat balance equation we must identify all the sources of heating of the system. We shall examine them for the S_2 island of a $S_1IS_2IS_1$ system. In this case, the island is deposited on a silicon substrate in thermal contact with the heat bath of a cryostat at temperature T_{bath}, the bath exchanges heat with the substrate which, in turn, exchanges heat with lattice phonons of the metallic island. One contribution to the heat balance equation for the island electron gas is thus heat exchange with the lattice phonons by the electron-phonon interaction, which is suppressed but never completely absent. Electrons can also exchange energy with the electromagnetic environment by electron-photon interaction, and this constitutes another contribution. Finally, the superconducting reservoirs (S_1) are in contact with the island through tunnel junctions. By applying a bias voltage V_c to the reservoirs we can extract and inject quasiparticles from and into the island, each having its own energy E, thus modifying the heat flow in a controllable way. By choosing a control bias voltage V_c we can set the heat flow between the island and the reservoirs. Then the energy conservation between this source of heat and the other two heating mechanisms (e-e and e-ph) allow the determination of the electronic temperature. Once the electronic temperature T_e versus the extraction voltage V_c is known, the distribution is completely specified by (1.11) and all the other observable quantities such as superconducting gap and Josephson current can be computed.

The heat exchanged with the reservoirs can be determined from the expression of the S_1IS_2 tunnel current (1.8). Multiplying the integrand times the energy E
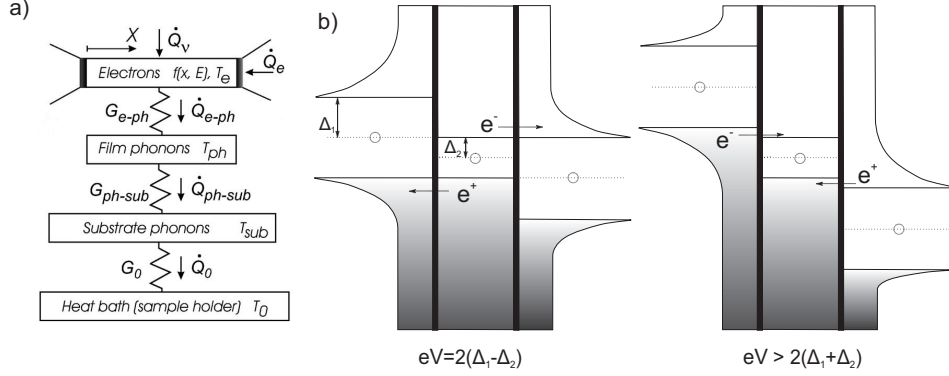
Figure 1.10: Panel (a) Thermal model of an electronic system characterized by electronic temperature T_e (top) in thermal contact with conductances G_{xx} with its phonon lattice, substrate and thermal bath (downward). In addition, heat can be exchanged between the sample and the reservoirs ($\dot{Q}_e$), electromagnetic environment ($\dot{Q}_\nu$), and lattice phonons ($\dot{Q}_{e-ph}$), the latter being thermalized with the heat bath through the substrate. Adapted from [12]. Panel (b) Semiconductor model for a $S_1IS_2IS_1$ junction. The first scheme corresponds to optimal cooling configuration, where hot quasiparticles are extracted from both reservoirs. The second configuration corresponds to the threshold voltage after which hot quasiparticles are injected in the central island, therefore het is injected in the island.

carried by each quasiparticle [9, 10, 12]:

$$\mathcal{P}^{S_1IS_2}(V_c) = \frac{1}{R_N e} \int_{-\infty}^{\infty} D_1(E - eV_c/2)D_2(E)[f(E, T_e) - f(E + eV_c, T_1)]EdE,$$

(1.19)

where T_1 is the temperature of the reservoirs S_1 and $D_{1,2}$ are the smeared BCS density of states (1.9) containing an appropriate γ to account for quasiparticle states within the gap. $\mathcal{P}^{S_1IS_2}(V_c) < 0$ means that heat is flowing from S_1 to S_2 (heating), while $\mathcal{P}^{S_1IS_2}(V_c) > 0$ means that heat is extracted from S_2 (cooling). The latter case is possible only if $\Delta_1 > \Delta_2$. The heat current is even in V_c so that $\mathcal{P}^{S_1IS_2}(V_c) = \mathcal{P}^{S_1IS_2}(-V_c)$, thus in the hypothesis of tunnel junctions with identical normal-state resistance R_N, the total heat current $\mathcal{P}(V_c)$ flowing from the central superconductor is obtained by multiplying $\mathcal{P}^{S_1IS_2}$ by two [13]. The behavior of the heat current is analogous to (1.8) and is shown in Fig. 1.11. $\mathcal{P}$ is monotonically increasing up to the logarithmic singularity (see Sec. 1.2) occurring at $eV_c = 2(\Delta_1 - \Delta_2)$, where the cooling power is maximized by the divergencies in the density of states of the superconductors. Heat is extracted (i.e., $\mathcal{P}(V_c) > 0$) until an abrupt drop occurs at $eV_c = 2(\Delta_1 + \Delta_2)$, at this voltage there is no cooling and hot excitations can tunnel back into the island [see Fig. 1.10(b)].

The lowest temperature that a mesoscopic island can attain by extraction of
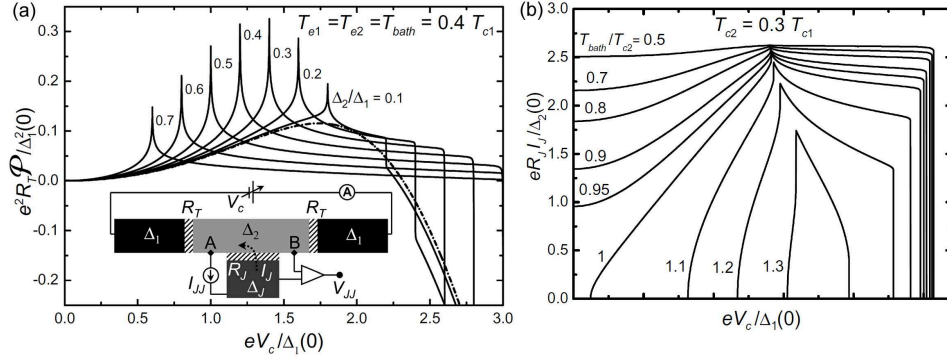
Figure 1.11: Panel (a): Heat extracted by a $S_1IS_2IS_1$ control line versus bias voltage V_c for different gap ratios at $T = 0.4T_{c1}$. The dash-dotted line represents heat flow in a SINIS control line. The heat current displays a sharp peak corresponding to the logarithmic singularity at $eV_c = 2(\Delta_1 - \Delta_2)$. Panel (b): Calculated Josephson current flowing between the central island and an additional tunnel contact labeled J (see the inset in left panel) versus injection voltage V_c applied to the $S_1IS_2IS_1$ line. Results are shown for different bath temperatures above and below the critical temperature of the island T_{c2} and for a gap ratio $\Delta_2/\Delta_1 = 0.3$. The smearing parameter $\gamma_{1,2}$ in the density of states of each superconductor is set to $10^{-4}\Delta_{1,2}$. Adapted from [13].

hot quasiparticles is determined also by other heat conduction mechanisms driving power into the system: the thermal exchange with the lattice phonons and with the electromagnetic environment. The heat transferred through both interactions depends on the difference between the electronic temperature and the one of the lattice or the electromagnetic environment. The electron-photon heat flux depends on their square powers [30, 12]:

$$\mathcal{P}^{e-\gamma}_{coll} = r\frac{k_B^2\pi^2}{6h}(T_e^2 - T_\gamma^2), \tag{1.20}$$

where $r = 4R_eR_\gamma/(R_e + R_\gamma)^2$ is a coupling constant with the electronic environment which depends on the resistances characterizing the electronic system (R_e) and the electromagnetic environment (R_γ). The electron-phonon heat flux depends on the fifth power of the temperatures [34]:

$$\mathcal{P}^{e-ph}_{coll} = \Sigma\mathcal{V}(T_e^5 - T_{ph}^5), \tag{1.21}$$

where Σ is a material-dependent constant of the order of 10^9W m^{-3} K^{-5} and $\mathcal{V}$ is the volume of the system. With the assumption $T_\gamma = T_{ph} = T_{bath}$, the electron-photon

heat flux is expected to become dominant only for very low electronic temperatures. However, perfect electromagnetic coupling ($r = 1$) is never met in the experimental conditions of this thesis and it is reasonable to assume $r = 0$ and consider as a limiting factor only electron-phonon interaction [29, 23]. The final energy balance equation is thus

$$\mathcal{P}(V_c, T_e, T_{bath}) + \mathcal{P}^{e-ph}_{coll}(T_e, T_{ph}) = 0, \tag{1.22}$$

from which by setting $T_{ph} = T_{bath}$ we can determine T_e for any injection voltage V_c. Once the electronic temperature is known, the Josephson current can be calculated from the Ambegaokar-Baratoff equivalent expression (1.18) [13]. The results for different bath temperatures are plotted in Fig. 1.11(b) for a gap ratio $\Delta_2/\Delta_1 = 0.3$ and $\gamma_{1,2} = 10^{-4}\Delta_{1,2}$. The plot shows that with these parameters a supercurrent can be generated at bath temperatures up to 1.3 times the critical temperature of the inner island. The optimal cooling bias where this happens is $V_c = 2(\Delta_1 - \Delta_2)/e$, and corresponds to the current peak in Fig. 1.11(b), which shifts according to the temperature dependance of Δ_1 and Δ_2. The supercurrent peak is visible for temperatures down to $T_{bath}/T_{c2} = 0.5$ where the zero injection value of the supercurrent is already saturated and no enhancing by quasiparticle extraction is possible. It is worth to anticipate that, as we will show in Chapter 4, introducing a larger smearing parameter γ in the density of states produces heating at low injection voltages, so that there is always a voltage range between zero and $eV_c = (\Delta_1 - \Delta_2)$ in which the supercurrent is suppressed even at the lowest temperatures.

The behavior of the Josephson current analyzed within the quasiequilibrium and nonequilibrium models shares some common features, namely the generation of the critical current above the critical temperature of the island and its suppression for certain voltage ranges even at bath temperatures below T_{c2}. A peculiar feature of the nonequilibrium model is the presence of hysteresis in the critical current versus injection. Another difference is in the voltage bias which maximizes the cooling power, which occurs at $eV_c = 2\Delta_1$, rather than at $eV_c = 2(\Delta_1 - \Delta_2)$ as in the quasiequilibrium model. In Chapter 4 we shall use the latter to analyze the experimental data presented in this thesis.

Chapter 2

Controllable Josephson junctions

In this chapter we will give an overview on some of the experimental work published on out-of-equilibrium phenomena and electron cooling in superconducting systems, showing what was the state of the research at the beginning of this project, and the different approaches that were explored to realize controllable superconducting junctions.

As shown in Chap. 1, electron tunneling can be used to control the distribution function of a metal by changing the occupation of the energy levels with respect to their equilibrium values, producing effects on observable quantities like supercurrent. A generic controllable Josephson junction is made up of two main parts: a control line used to bring a metallic island out of equilibrium, and a probe line which shares the same metallic island (see Fig. 2.1). Controllable tunneling devices are usually fabricated by nanolithography and shadow mask evaporation, a technique that allows good reliability and flexibility in the fabrication of tunnel barriers (see Chapter 3). The device is cooled to low temperature, where experiments are performed by varying the voltage bias in the control line and observing the effect of some measurable quantity through the probing line. This can be used, for instance, to achieve electronic refrigeration of a metallic island, or to control the Josephson current flowing through it through a probing superconducting line. By recording full current-voltage characteristics in the probing line it is also possible to extract information on the distribution function of the island. For example, in the case of electronic refrigeration, the electronic temperature can be monitored by studying
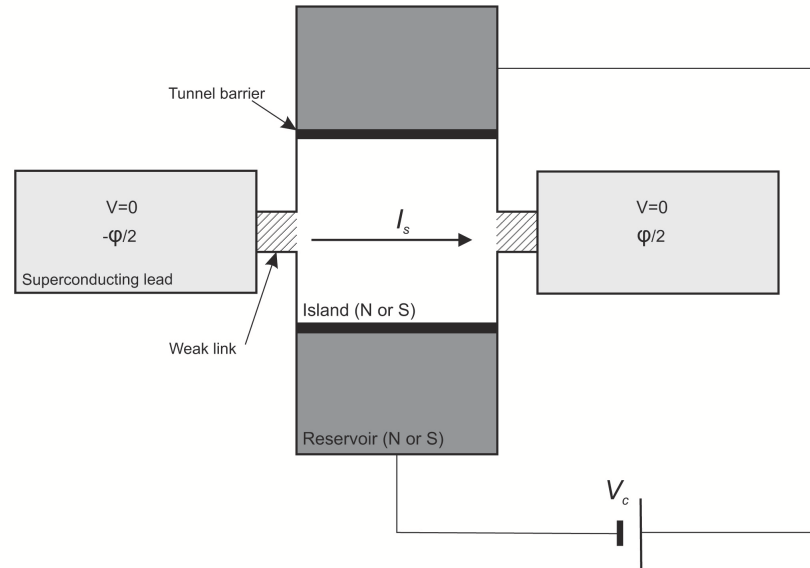
Figure 2.1: Generic scheme of a controllable Josephson junction. The reservoirs (dark grey) act as a control line for the central island which they are in contact with through tunnel barries (black). V_c is the control voltage applied to the reservoirs, and I_s is the supercurrent flowing between the superconducting leads (light grey). The dashed area connecting the superconducting leads can be any weak link such as a tunnel barrier or a normal metal constriction for SNS controllable junctions, and ϕ is the phase difference between the supeconductors.

any temperature-dependent quantity in the probing tunnel junctions. This chapter will present some examples of Josephson junctions used both for transistor-like devices and as electronic refrigerators.

2.1   Normal metal control line

One of the possible approaches to fabricate a controllable Josephson junction is based on a normal-metal control line. This approach was successfully demonstrated in Ref. [24] and [2], where the authors used gold for the normal-metal parts and niobium as a superconductor. The control line was made of two gold reservoirs with a cross-shaped mesoscopic gold wire as a weak link, which constituted the region to be driven out of of equilibrium. A niobium-gold superconductor-normal metal-superconductor (SNS) Josephson junction was fabricated by sputtering, the normal metal being the mesoscopic gold wire shared by the control line. An outline of this device is shown in Fig. 2.2(a). Such a SNS junction can sustain a supercurrent thanks to Andreev reflections occurring at the SN interfaces. The su-
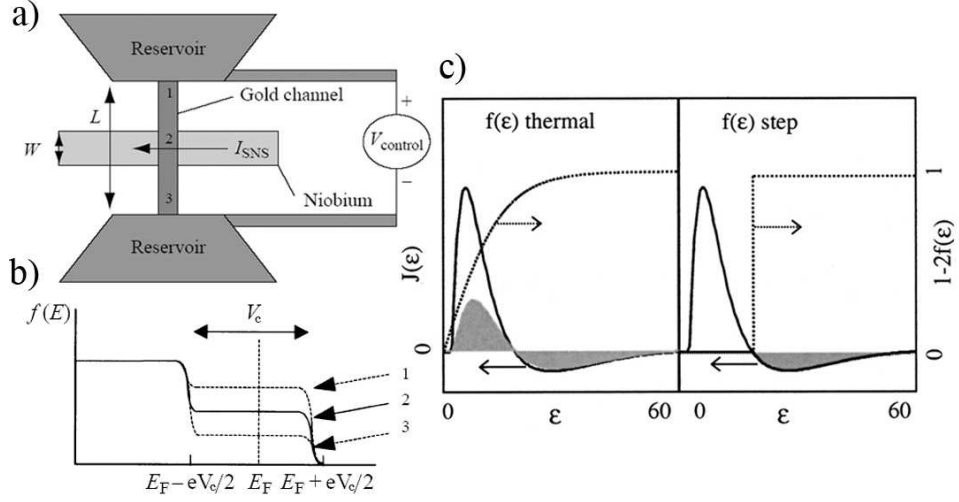
Figure 2.2: Panel (a): Outline of the niobium-gold SNS device with a normal metal control line, biased through the voltage bias V_c. 1,2 and 3 indicate the point where distribution function is shown in (b). Panel (b): Out-of-equilibrium distribution function produced by a normal control line at different points of the central island (1,2,3) of panel (a). Panel (c): Plots of supercurrent carrying density of states $J(\varepsilon)$ (solid line) and $1 - 2f(\varepsilon)$ versus energy normalized to the Thouless energy $\varepsilon = E/E_{Th}$ for a quasi 1-dimensional diffusive wire. The gray shaded areas show the occupation of the supercurrent carrying states. For a thermal distribution (left panel) the occupied positive current carrying states are more than the negative ones. For a double-step distribution function (right panel) only the negative ones can be occupied, which allows to observe an inversion of the sign of the critical current. Adapted from [3, 4].

percurrent was controlled by applying a voltage bias to the big gold reservoirs of the control line. The reservoirs are supposed to be well thermalized with the substrate, and to remain at equilibrium while a voltage bias is applied across them. When one reservoir is biased at $-V_c/2$ and the other at $+V_c/2$, the Fermi level potentials shift accordingly. So if $f_0(E, E_F)$ is the distribution function at the equilibrium with no bias voltage (Eq. 1.11), the distribution function in the reservoirs becomes $f_0(E, E_F + eV_c/2)$ and $f_0(E, E_F - eV_c/2)$, respectively. In the absence of inelastic relaxation, the distribution function $f(E)$ in the middle of the constriction which connects the two reservoirs is equal to the average of their distribution function, i.e.:

$$f(E, V_c) = \frac{1}{2} \left[f_d(E - eV_c/2) + f_d(E + eV_c/2) \right].$$ (2.1)

The distribution function is position-dependent, tending to the Fermi function of the closest reservoir as we move along the lenght of the constriction [see Fig. 2.2(b)].

The SNS junction is fabricated so that the superconducting leads are very narrow and the normal part involved in electrical conduction is just the middle section of the gold constriction. The distribution function inside the active normal part of the SNS junction is then assumed to be expressed by Eq. 2.1.

The shape of the distribution function influences the current flowing in the SNS line by modifying the occupation of the so-called *current-carrying Andreev bound states*. Andreev reflection is a process that occurs at the interface between a normal metal and a superconductor: an impinging electron propagating from the normal metal can be reflected as a hole at the interface, with the transport of a charge $2e$ inside the superconductors, i.e., the creation of a Cooper pair. In presence of two interfaces, electron and holes can undergo multiple reflections and create "bound states" that carry a net supercurrent. In a quasi-1D diffusive wire, electron and holes wavefunctions bouncing back and forth from the NS interfaces acquire different phase differences according to their energies and travelled path, producing positive and negative current-carrying states. The full line in Fig. 2.2(c) shows the profile of the total current-carrying density of states $J(E)$ (spectral supercurrent) which takes into account all the possible paths that contribute to coherent trasport in the case of a long wire (i.e, $L > \xi_0$ where L is the length of the N wire and ξ_0 is the coherence length in the superconductor forming the SNS junction). $J(E)$ is plotted versus energy normalized to the Thouless energy $E_{Th} = \hbar D / L^2$, where D is the diffusion constant in the wire and L is its length, which is the typical correlation energy in diffusive conductors. Only the positive branch is shown, as $J(E)$ is an odd function in E. Above a zero contribution threshold, the low-energy states carry a positive supercurrent, while in the intermediate energy range around $E \approx 20 E_{Th}$ the Andreev bound states carry a negative supercurrent. The total supercurrent in the SNS diffusive junction is found by integrating over all the possible energies according to the following expression [2]:

$$I_c = \frac{1}{R_N} \int_0^{+\infty} [1 - 2f(E)] J(E) dE, \tag{2.2}$$

where R_N is the resistance of the normal metal wire and $f(E)$ is the distribution function inside it. This expression shows that the value of $1 - 2f(E)$ determines which states play an active role in carrying the supercurrent and which ones are suppressed. Therefore we can act on the supercurrent by inducing an out-of-equilibrium distribution function that suppresses, for example, all the positive contribution to the supercurrent. In Fig. 2.2(c) the quantity $1 - 2f(E)$ is plotted in the
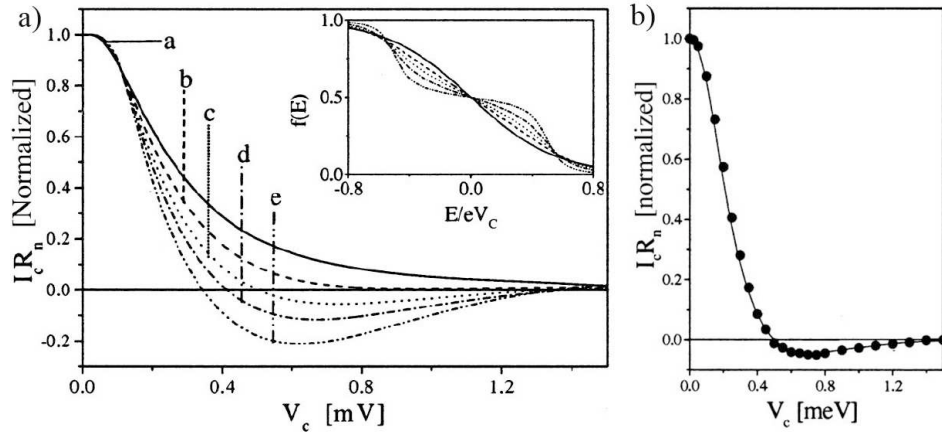
Figure 2.3: Panel (a): Theoretical prediction for the critical current in a SNS diffusive junction versus injection voltage for different relaxation strength: line "a" corresponds to strongest relaxation, line "e" to weakest. The inset shows the corresponding effect of increasing inelastic relaxation onto the double step nonequilibrium function. The distribution becomes more rounded with increasing relaxation, tending to a Fermi function. Panel (b): Experimental data for a gold-niobium controllable π-junction. Note the sign reversal of the supercurrent (π-shift) at 0.52 mV. Adapted from [4].

cases of a thermal distribution and a out-of-equilibrium double-step profile. The occupation of the Andreev bound states is represented by the gray shaded area. In case of the double-step profile as Eq. 2.1, there is an energy range of width eV_c, corresponding to the central step of the distribution function shown in Fig. 2.2(a), where $[1 - 2f(E)] = 0$ and all the states of corresponding energy are suppressed. Therefore, with such a distribution function there is a value of V_c at which only negative states give their contribution to the supercurrent. This produces a sign reversal, and is called a π-shift.

When some inelastic relaxation is present, the double-step profile of the distribution function becomes increasingly smeared and tends to a thermal distribution. Figure 2.3(a), shows the theoretical prediction for the critical current I_c in the SNS junction versus control voltage V_c for different electron-electron inelastic relaxation strengths. Line "e" shows the supercurrent versus control voltage dependence for very small inelastic relaxation. In this case for large enough V_c all the positive contributions to the supercurrent are suppressed and the critical current reverses its sign undergoing a π-shift. As inelastic relaxation increases (lines from "d" upwards), the double-step profile of the distribution function gets more smeared and it becomes impossible to completely suppress the positive contributions to the current, therefore the π-shift disappears [line "b" in Fig. 2.3(a)]. Figure 2.3(b) shows

30

the experimental result for a gold-niobium π-junction with normal-metal weak link of 300 nm x 1 μm, the shorter being the length of the SNS channel. The condition on the length of the weak link to be much smaller than the electron-electron scattering length does not hold rigorously in a sample with these characteristics [2]. However the data show nonetheless that relaxation is suppressed enough to induce nonequilibrium in the normal metal constriction and realize a π-shift at $V_c \approx 0.52$ mV.

2.2 SINIS junctions

Another approach than can be used to drive a metal out of equilibrium is the implementation of a superconductor-insulator-normal metal symmetric junction (SINIS). The use of SINIS control line opens more possibilities for applications than the fully normal metal control line. SINIS-type junctions were theoretically investigated for their implementation as transistor-like devices, both in the nonequilibrium and quasiequilibrium limit [11]. In addition, they have been implemented as nanorefigerators, both for electron [21, 27, 29] and lattice cooling [7, 22].

SINIS transistors

A SINIS control line is able to produce nonequilibrium distribution functions strongly deviating from a thermal profile [see Fig. 1.7(a)] and can extract heat very efficiently. Because of these features, SINIS junctions are of interest as control lines for SNS Josephson junction transistor as analyzed in Ref. [11]. Figure 2.4 shows the predicted behavior of the Josephson current in the SNS line of a SINIS-controlled Josephson transistor. The critical current is calculated from (2.2), and Fig. 2.4(a) shows a plot of $1 - 2f(E)$ together with the occupations of the current-carrying Andreev bound states in the SNS junction (dashed areas). The use of a SINIS junction produces an enhancement of the critical current which is not present in the case of a normal control line. At the corresponding injection voltage $V_c \approx 2\Delta/e$ [point labeled (I) in Fig. 2.1(a)], the out-of-equilibrium distribution function is sharp, zero-temperature like [see Fig. 1.7(a)], therefore the current enhancement can be interpreted as a cooling effect. At higher injection voltages a π-shift is observed, where the critical current becomes negative (region labeled (II) in Fig. 2.1). In the case of a SINIS control line, the magnitude of the π-current is about two times larger than observed in an all-normal control line. This is caused by the peculiar shape of
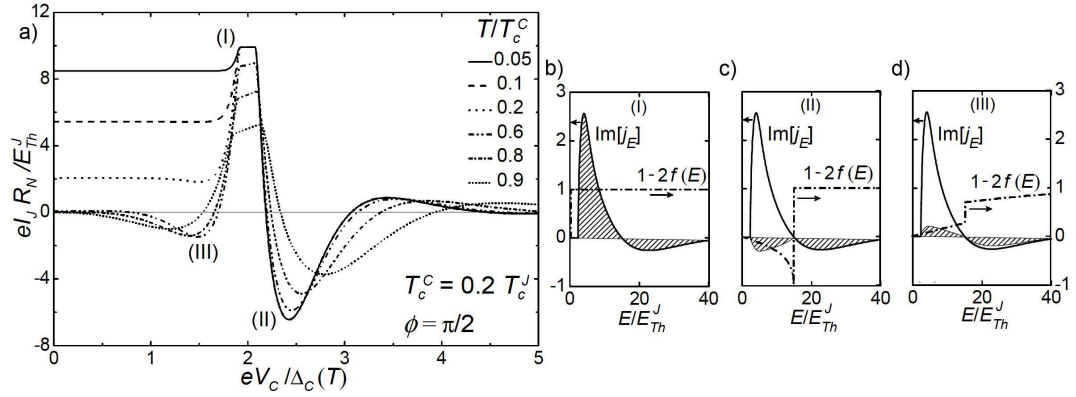
Figure 2.4: Panel (a): Theoretical prediction for the supercurrent versus injection voltage for a SINIS-controlled Josephson transistor at different bath temperatures. Δ_c and T_c^C are superconducting gap and critical temperature of the reservoirs respectively, and T_c^J is the critical temperature of the leads of the SNS junction. The supercurrent is normalized to the Thouless energy E_{Th}^J and normal-state resistance of the junction. Panel (b,c,d): Spectral supercurrent (solid line) and population of current carrying states (dashed area) under different injection conditions, corresponding to injection values indicated by labels (I), (II), (III) in panel (a). Dash-dotted line shows $1 - 2f(E)$ for each injection value. Adapted from [11].

the nonequilibrium distribution function for control voltages $V_c > 2.5\Delta/e$ [see Fig. 1.7(a)], that allows not only to suppress the positive current carrying states, but also to negatively bias them, as the term $1 - 2f(E)$ in (2.2) can be made negative for those states [see Fig. 2.4(c)]. Another peculiar feature of this type of device is the observation of a small π-state at low injection voltages [region (III) in Fig. 2.1] whose existence can be understood by inspecting the shape of the distribution function for $eV_c/\Delta = 0.5$ in Fig. 1.7(a), noting its similarity with the smeared double-step profile achieved with a normal control line [see inset of Fig. 2.3(a)]. A distribution function with such a profile, as we have shown in the previous section, suppresses the positive current-carrying states and produces a π-shift.

So far the only experimental demonstration of a SINIS control line for transistor-like operation was reported from A. Savin *et al.* [29], in an Al/AlO$_x$/Cu device, shown in Fig. 2.5(a). A control voltage V_c was applied to the injector junctions of the device, while the critical current was measured through the two smaller inner junctions. A selected dataset from this work is presented in Fig. 2.5(a). Data show enhancement and suppression of the critical current upon varying V_c, but no π-shift is observed. Authors claim that this absence was due to strong electron-electron
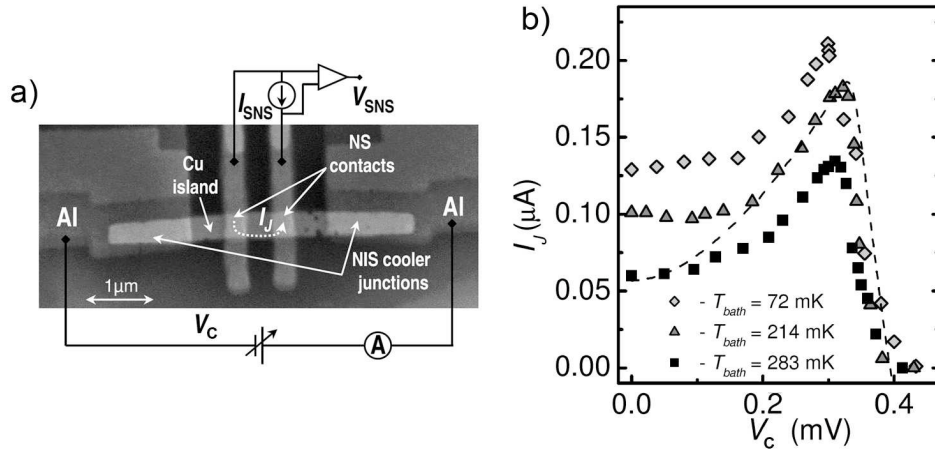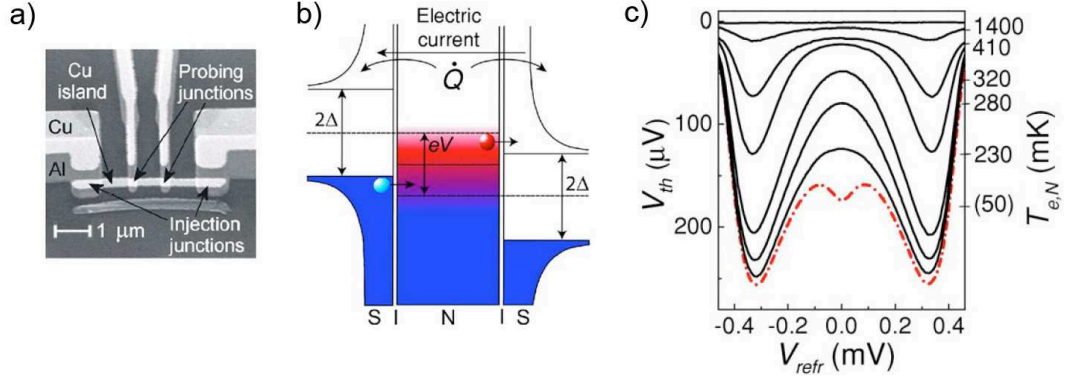
Figure 2.5: Panel (a): Scanning electron micrograph of the SINIS controllable junction and measurement setup. Panel (b): Supercurrent in the SNS line of a controllable Al/Cu SINIS transistor at three different bath temperatures. The dashed line shows the theoretical prediction for the Josephson current. Adapted from [29].

relaxation in the device which drove it into the quasiequilibrium regime, so that the distribution function retained a thermal-like profile. Supercurrent enhancement and suppression were thus interpreted in terms of cooling and heating of the normal island. The authors used the heat balance equation (1.22) to determine the electronic temperature of the normal island and the distribution function inside it, which can be inserted into (2.2) to calculate the supercurrent. The predicted behavior of the supercurrent was in qualitative agreement with the observed data [see dashed line in Fig. 2.5(a)].

SINIS coolers

The use of SINIS junctions as solid-state refrigerators is more documented than their implementation as superconducting transistors. As shown in Sec. 1.3.2, superconducting junctions can be effective as quasiparticles refrigerators in the quasiequilibrium limit. SINIS devices to be used as coolers are thus fabricated so that strong inelastic electron-electron relaxation is present in the normal region. Figure 2.6(a) shows an implementation of a SINIS electron refrigerator based on copper and aluminum. The control voltage V_c applied to the injector junctions allows to modify the electronic temperature of the normal region by extraction of hot quasiparticles.
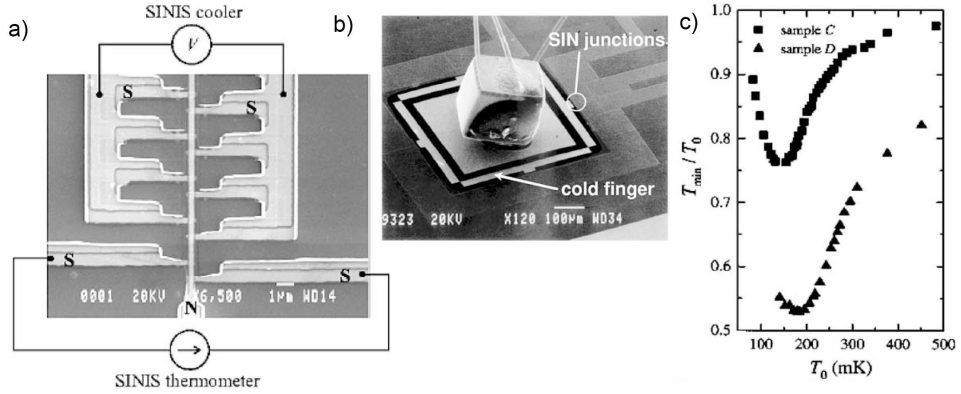
Figure 2.6: Panel (a): Scanning electron micrograph of an Al-AlO$_x$-Cu-AlO$_x$-Al SINIS structure. Panel (b): Semiconductor model for a SINIS refrigerator, showing cold quasiparticle injection below the Fermi energy from the left, negatively biased reservoir and hot quasiparticle extraction to the right one. Both junctions act as coolers. Panel (c): Data from the sample shown in panel (a), demonstrating strong cooling down to the base temperature of the cryostat. The right axis shows the temperature obtained from the calibration of the SINIS probes used as thermomethers. (b) adapted from [12]; (a) and (c) adapted from [27].

A crucial task in these kinds of experiments is the determination of the electronic temperature of the normal region. In principle, every temperature-dependent quantity may be used for thermometry. A common approach (see e.g., Ref. [27]) is to use two additional NIS probing junctions as thermometers [see Fig. 2.6(a)]. A small constant current is driven through them, and from the reading of the voltage drop developed across the SINIS line that they form it is possible to determine the electronic temperature of the normal junction. This can be understood by inspecting the expression for the NIS current presented in Sec. 1.2:

$$I^{NIS} = \frac{1}{R_N e} \int_{-\infty}^{\infty} \frac{|E|}{\sqrt{E^2 - \Delta^2}} [f(T_e, E) - f(T_{bath}, E + eV^{NIS})]dE. \qquad (1.7)$$

In this equation, T_{bath} is the temperature of the thermal bath, which is assumed to be known, the only variables are thus the current I^{NIS} through the junction, the voltage V^{NIS} across it, and the electronic temperature T_e. Thus, if the values of I^{NIS} and V^{NIS} are determined by measurement, it is possible to extract the corresponding electronic temperature by solving (1.7) in T_e. Experimentally, the electronic temperature is obtained performing a calibration of V^{NIS} versus T_{bath} at the equilibrium. To do this, I^{NIS} is set to a fixed value throughout the experiment, and V^{NIS} is measured while varying the bath temperature which, being at the equilibrium, is assumed to be the same as the electronic temperature of the normal metal. This

Figure 2.7: Panel (a): Multiple SINIS junction used to cool down the long vertical normal island. The bottom SINIS junction is used for thermometry. Panel (b): Scanning electron micrograph of a SINIS-cooled suspended Si_3N_4 membrane. The normal region of a SINIS junction extends on each side of the Si_3N_4 square membrane through self-suspended bridges. The big cube is a Ge thermometer used to measure lattice temperature in addition to two NIS junctions in the middle of the membrane (not visible). Panel (c): Data from lattice cooling of a suspendend membrane from two samples with different performances. (b) adapted from [7]; (a) and (c) adapted from [22].

procedure thus provides the relation between T_e and V^{NIS} to be used throughout the experiment for the thermometry. The use of NIS junctions for thermometry has the advantage that thermometers can be fabricated in the same processing step as the device, and given their small size one or more thermometers can be integrated in the device. The drawback is that their sensitivity is much reduced at low temperatures (typically below 50 mK) that may be accessible with SINIS refrigerators [12].

Figure 2.6(c) shows cooling data a different bath temperatures for the Al-AlO$_x$-Cu refrigerator of Ref. [27] which uses this kind of thermometry. A pronounced cooling dip around $V_c \approx 2\Delta/e$ is present at all temperatures but the extracted heat is maximized at $T = 0.25\Delta/k_B$ (in this case ≈ 300 mK) [12]. At the lowest bath temperature the cooling curve shows a heating-cooling-heating behavior caused by a finite quasiparticle density of states within the gap [i.e., a finite smearing parameter γ in (1.9)], which is one of the limiting factors for the minimum temperature achievable with a SINIS refigerator [27].

Other factors that influence the minimum achievable electronic temperature with a SINIS refrigerator are the normal-metal island volume and the normal-state resistance of the tunnel junctions. The specific resistance of the junction should be

as small as possible, but this is not easy to achieve since natural oxide junctions with low specific resistance tend to be affected by defects in the dielectric (pinholes). Low normal-state resistances may be achieved by widening the junction area, but this may impair the effectiveness of the SINIS cooler because of quasi-particle backtunneling. This happens because when large junctions are used for extraction, quasiparticles need more time to escape from the junction area, and it is more likely that a high concentration of quasiparticles accumulates close to the junction. Having a high density of quasiparticle in proximity of the barrier may produce back-tunneling and subsequent heating of the normal island [18]. A possible approach to limit backtunneling in large-area junctions is to use many junctions with smaller areas to maximize the junction-area to normal-volume ratio. This was done in Ref. [22] and a micrograph of a device of that kind is shown in Fig. 2.7(a).

Another relevant application for SINIS refrigerators is lattice cooling. In this class of devices, the cooled normal region of the SINIS junction extends onto a suspended Si_3N_4 membrane [see Fig. 2.7(b)]. The normal region is cooled by quasiparticle extraction and its lattice phonons are also cooled by electron-phonon interaction. The suspended membrane is then cooled by phonon-phonon interaction with the phonons of the normal metal region deposited on top. For this last heat-conduction step, the contact area between the membrane and the normal metal is very important. Power is exchanged between them according to the Kapitza coupling [28]:

$$\mathcal{P}_K(T_{ph}, T_{sub}) = KA(T_{ph}^4 - T_{sub}^4), \qquad (2.3)$$

where T_{ph} and T_{sub} are the lattice phonon and membrane temperature respectively, K is a material-related constant and A is the contact area between the membrane and the normal metal, which needs to be maximized for best performances, the normal-metal region is thus rather wide to maximize the contact area with the membrane. With this approach lattice cooling of the membrane was demonstrated by measuring its temperature both with integrated NIS junctions and with a bulk external thermometer in contact with the membrane [see Fig. 2.7(b)]. A device of this kind was presented in Ref. [7]. Lattice cooling down to 240 mK from a starting temperature of 320 mK was demonstrated. Ref. [22] also demonstrated lattice cooling in a suspended device down to 50% of the starting temperature of 200 mK with an estimated cooling power in the pW range. A dataset from this work is presented in Fig. 2.7(c), showing the minimum temperature achieved (T_{min}) versus starting bath temperature (T_0) for two SINIS devices on suspended membranes.

Recently Rajauria *et al.* [28] also found hints of electron-phonon coupling and phonon cooling at temperatures down to 292 mK with a SINIS fabricated on an unsuspended silicon substrate, having a normal island of size 5 μm $\times$ 1.5 μm $\times$ 50 nm.

2.3 All-superconducting structures

In this section we shall present more in detail experimental work that was published on out-of-equilibrium all-superconducting devices, which are the focus of this thesis. The first experimental demonstration of gap enhancement through extraction of quasiparticle was realized in 1979 [6], but lille experimental work on $S_1IS_2IS_1$ tunnel junction was published afterwards. Recently, $S_1IS_2IS_1$ structures regained attention for their use as quasiparticle refrigerators.

The first implementation of a $S_1IS_2IS_1$ structure to induce nonequilibrium was performed by Chi and Clarke [6] in 1979. Their device was a three layers stack of aluminum, fabricated in three different evaporation steps. The layers were 3mm wide strips deposited slanted by about $45°$ so that they overlapped only in the middle part. The central superconducting layer (S_2) was evaporated with a lower vacuum than the other to have lower critical temperature. The measuring and control lines in this device were not symmetric: rather than two $S_1IS_2IS_1$ junctions as depicted in Fig. 2.1, two single S_1IS_2 junctions were used separately, one for extraction/injection and the other for measurement, S_2 being shared between the two. The first S_1IS_2 junction was voltage-biased, and the curent-voltage characteristic of the other one was measured. The gap of the S_2 region was inferred by the observation of the features at voltages $(\Delta_1 - \Delta_2)/e$ and $(\Delta_1 + \Delta_2)/e$ in the current-voltage characteristics. Figure 2.8(a) shows the differential conductance of the probing S_1IS_2 junction, where features at $(\Delta_1 - \Delta_2)/e$ and $(\Delta_1 + \Delta_2)/e$ are easily seen. Curves labeled from "a" to "e" were taken at progressively higher voltage bias, with "d" corresponding to the optimal extraction bias for a single junction ($V_c = (\Delta_1 - \Delta_2)/e$) [see Sec. 1.3.2]. The (slight) shift to lower energies of $(\Delta_1 + \Delta_2)/e$ and that to higher energies of $(\Delta_1 - \Delta_2)/e$ at this bias was interpreted by the authors as a gap enhancement of S_2 due to quasiparticle extraction. Authors reported observation of gap enhancement up to 40% at $T = 0.986 T_{c2}$, where $T_{c2} = 1.35 K$ was the central aluminum layer (S_2) critical temperature.

A similar experiment was also performed by Blamire *et al.* [5], with the fabrication of a $S_1IS_2IS_1$ junction made with niobium as the larger gap superconductor
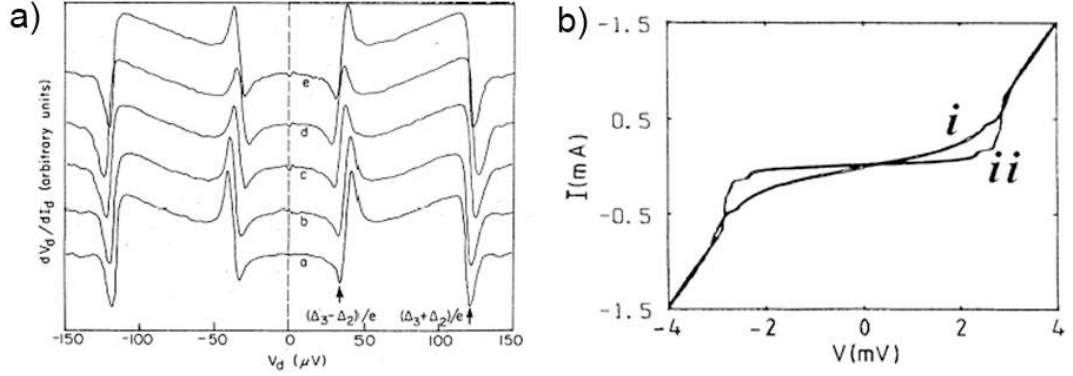
Figure 2.8: Panel (a): Differential conductance data of the probing S_1IS_2 junction from Ref. [6]. Data were taken at $T_{bath} = 0.986T_{c2}$, for the central S_2 aluminum layer $T_c = 1.35K$. Panel (b): Current voltage characteristic of the $S_1IS_2IS_1$ junction measured in Ref. [5]. "i" is measured at 4.2 K and "ii" at 2.2K. The small step seen just before the quasiparticle onset is addressed by the authors as a sign of aluminum superconductivity. (a) adapted from [6]; (b) adapted from [5].

and aluminum as central island. In this experiment one single, symmetric $S_1IS_2IS_1$ junction was used for both quasiparticle extraction/injection and measuring. This was done by driving the junction with an AC current spanning the relevant voltage range ($|V_c| \gtrsim 2(\Delta_1 + \Delta_2)/e$). Being a single junction, quasiparticles were effectively extracted from the S_2 layer only when the junction was biased with a voltage $V_c \approx 2(\Delta_1 - \Delta_2)/e$. This is also the voltage at which a logarithmic singularity appears in the current-voltage characteristic (see Sec. 1.2), which is present only if S_2 is in its superconducting state. The logarithmic singularity appeared in the I-V characteristichs as a notch just before the onset at $V_c = 2(\Delta_1 + \Delta_2)/e$ [see Fig. 2.8(b)]. By observing the presence of this feature at temperatures much higher than its equilibrium critical temperature, the authors claimed that S_2 was driven into its superconducting state by self-extraction of quasiparticles. Bath temperature was varied from 2.2 K, slightly below the critical temperature of the aluminum film ($T_{c2} = 2.2 - 2.4$ K) to 4.3 K. Data obtained demonstrated gap regeneration up to 4.3 K, about twice the critical temperature of the aluminum film. A similar experiment was also performed more recently (1997) by Nevirkovets [25]. In all of the experiment presented, the gap enhancement was detected by looking at gap-dependent features in the current-voltage characteristics. Because of the experimental setup, Josephson current was never observed.
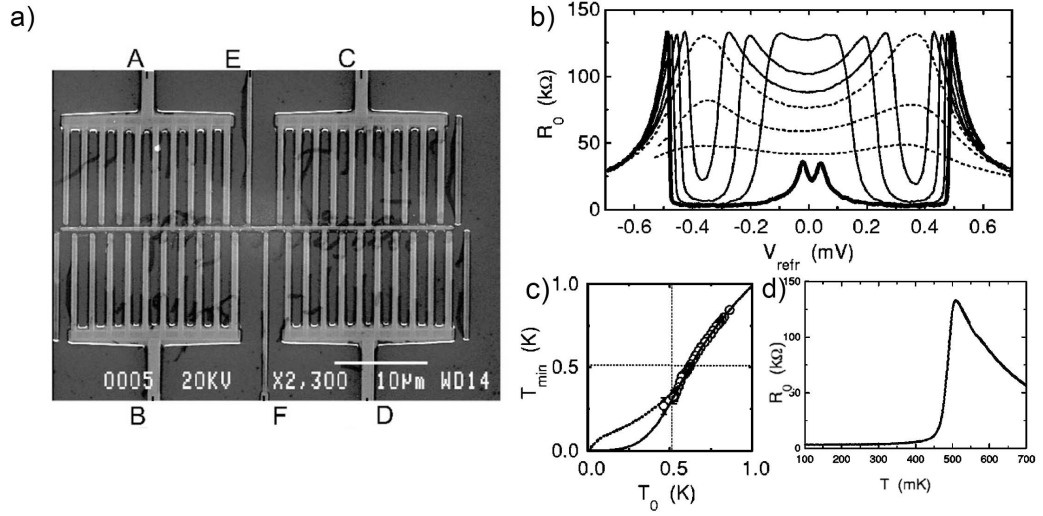
Figure 2.9: Panel (a): Scanning electron micrograph and measurement setup used in Ref. [23]. The two comb-shaped arrays of $S_1IS_2IS_1$ Al-Ti-Al junctions (A-B, C-D) act as a quasiparticle refrigerator, while the zero bias resistance (R_0) of an additional $S_1IS_2IS_1$ junction (E-F) is used for thermometry. Panel (b): Zero bias resistance of the E-F junction versus injection voltage V_{refr}. Dashed lines correspond to normal titanium (increasing R_0 corresponds to lower T_e), solid lines correspond to titanium being cooled below its superconducting temperature (decreasing R_0 corresponds to lower T_{Ti}), thick solid line has titanium in the superconducting state (R_0 almost insensitive to T_{Ti} variations). Panel (c): Minimum electronic temperature achieved versus bath temperature (open circles), minimum temperature calculated from (1.22) in the SINIS case (dotted line) and $S_1IS_2IS_1$ case (solid line). The straight horizontal and vertical dotted lines show titanium critical temperature. Panel (d): current-voltage characteristics used for calibration of the E-F junction used for thermometry. Adapted from [23].

A different experiment from the ones presented is shown in Ref. [23], which demonstrates an implementation of a $S_1IS_2IS_1$ structure as electronic refrigerator. The authors fabricated an array of Al/AlO$_x$/Ti junctions [see Fig. 2.9(a)] and used it to cool a strip of titanium by quasiparticle extraction. For thermometry they fabricated an additional junction whose zero-bias resistance was used to monitor the electronic temperature of the titanium film. The use of zero-bias resistance as a temperature-dependent quantity for thermometry prevents self-cooling of the probing junction. A full calibration was done by varying the bath temperature and measuring R_0. The dependence between R_0 and T is non-monotonic [see Fig. 2.9(d)], so the resistance versus injection data [Fig. 2.9(b)] must be interpreted accordingly. The observed behavior of R_0 versus injection voltage of the cooling junctions is shown in Fig. 2.9(b) for bath temperatures from about 900 mK down

39

to 480 mK, where titanium critical temperature was $T_c = 510$ mK. Solid lines show that titanium was cooled from the normal to the superconducting state, while dotted lines show cooling above its T_c and thick solid lines show almost no cooling, also because the thermometry used. Figure 2.9(d) shows that temperature sensitivity of R_0 is good around T_c but worsens at lower temperatures. Optimal cooling was achieved for $V_{refr} \approx 2\Delta_1/e = 420$ μeV, as in the SINIS case, which is relevant when titanium is in its normal state. The demonstrated titanium cooling by quasiparticle extraction was from 1.02 T_c down to 0.7 T_c. Authors used the heat balance equation (1.22) both for the SINIS and $S_1IS_2IS_1$ cases to fit their data [solid lines in Fig. 2.9(c)]. The fits show good agreement with the experiment in either case, as most of the experimental data were collected above T_c where the SINIS and $S_1IS_2IS_1$ cases are not distinguishable. This experiment also demonstrated the effectiveness of $S_1IS_2IS_1$ junctions as electronic refrigerators. Authors also pointed out some unexplained features with hysteretic behavior in the current-voltage characteristics which we also encountered in our experiment and will be examined in Chapter 4.

Chapter 3

Sample fabrication and experimental techniques

In this chapter we shall give an overview of the experimental techniques used to fabricate the $S_1IS_2IS_1$ junctions which are the focus of this work. Special attention was devoted to the optimization of the tunnel barriers and to the quality of evaporated films, which are crucial factors in the realization of the devices. The realization of the $S_1IS_2IS_1$ device led us to an improved understanding of the aluminum oxide tunnel barriers coupled with titanium.

3.1 Sample fabrication techniques

The samples presented in this work were fabricated using shadow-mask evaporation with a PMMA / PMMA-MA resist bilayer spun onto a Silicon substrate insulated by 500 nm of thermally-grown oxide, and two angle e-beam evaporation. Tunnel barriers were made by oxidation of an aluminum layer under constant pressure of pure oxygen in a separate chamber without breaking the vacuum. This section is a detailed description of the processing steps involved.

3.1.1 Electron beam lithography

E-beam lithography is a well established and reliable technique for the realization of nanostructures with a theoretical resolution down to a few nanometers. The standard lithography process involves the coating of a proper substrate, usually a silicon chip or a suitable semiconductor, with a Poly(Methyl Metha Acrylate) (PMMA)

of suitable thickness. PMMA is available in solutions so it can be spun onto the substrate with a spin coater, then the coated substrate is baked on a hot plate to evaporate the solvent. A focused electron beam controlled by a patterning software and hardware system is then used to pattern the surface of the PMMA film: the impinging electrons break the long polymer chains into smaller pieces, which can then be removed with a proper solvent. PMMA is available in different molecular weights: higher weight means longer polymer chains and a larger energy required to break them. The use of higher energies provides better resolutions in the patterning step. This step creates a positive mask on the PMMA layer defining the profile of the device. A metallic film is then deposited on the wafer. Finally, a solvent, usually acetone, is used to remove all the remaining PMMA on the substrate along with the metallic film which is not directly deposited on the substrate, leaving only the required patterned positive outline which constitutes the device. This last step is usually referred to as *lift off*.

A commonly used technique for the fabrication of tunnel junctions is shadow mask evaporation (see Fig. 3.1). This process requires the fabrication of a thick resist layer that can be patterned to create a suspended mask, with a hollow space underneath (undercut). This is achieved by coating the substrate with a multi-layer of PMMA. The conventional PMMA bi-layer uses two polymers with different molecular weight spun on the substrate one on top of the other: the bottom layer, more sensitive to the electron beam, is exposed by the forward scattering of the electron impinging on the top layer, and the divergence of the scattered beam creates a small undercut. Another type of bi-layer uses PMMA on top and the co-polymer Poly(Methyl Metha Acrylate-Methacrylic Acid) (PMMA-MA) on the bottom, which is even more sensitive to electron beam than low molecular weight PMMA. This system offers great flexibility in controlling the undercut: it is possible to create asymmetric undercuts by exposing the bi-layer with an electron dose small enough not to affect the top PMMA layer, but large enough to expose the co-polymer on the bottom.

To obtain a proper bilayer, one must pay special care in the spinning process: the bottom (co)polymer is often soluble in the top layer solvent and one must make sure that the top layer solvent is not strong enough, it is then necessary to spin the second layer rapidly enough to avoid intermixing at the interface. To completely avoid intermixing, it is also possible to use a more complicated process and create a tri-layer by depositing a germanium film between the two layers. A germanium
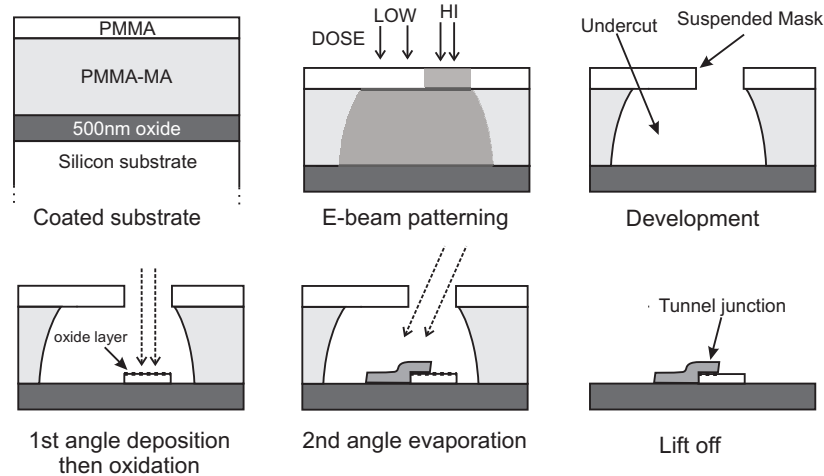
Figure 3.1: Processing steps for the fabrication of a tunnel junction device through shadow mask evaporation.

suspended mask can be fabricated by patterning the top PMMA layer and using reactive ion etching (RIE) to remove the exposed germanium.

PMMA / PMMA-MA bilayer

The substrate used was an undoped Silicon <100> wafer with 500 nm of thermally grown oxide. Whole wafers were coated to achieve maximum homogeneity in the resist thickness, then they were cleaved into smaller pieces for patterning.

Bottom layer: MicroChem EL13 PMMA-MA 8.5% in ethyl-lactate spun at 1500 rpm then baked at 170°C on a hot plate for 15 minutes. The obtained layer was test-patterned and measured with a Dektak profilometer. The resulting thickness was 1 μm, with slight changes depending on temperature and environmental condition. The homogeneity on a whole 3″ wafer was within 3-4%.

Top layer: MicroChem A4 PMMA 950 mw 4% in anisole spun at 3500 rpm then baked at 170°C on a hot plate for 15 minutes. The resulting thickness was about 130 nm.

Typical exposure doses were 300 $\mu C/$cm^2 for big features and up to 800 $\mu C/$cm^2 for smaller linewidths, and 50-100 $\mu C/$cm^2 to create undercut where necessary. Minimum achievable linewidths are as low as 25 nm.

Development of the exposed pattern was done with AR-P 600.56 developer, 3:1 IPA:MIBK for 20 seconds at 25°C. Temperature and developing time are quite cru-
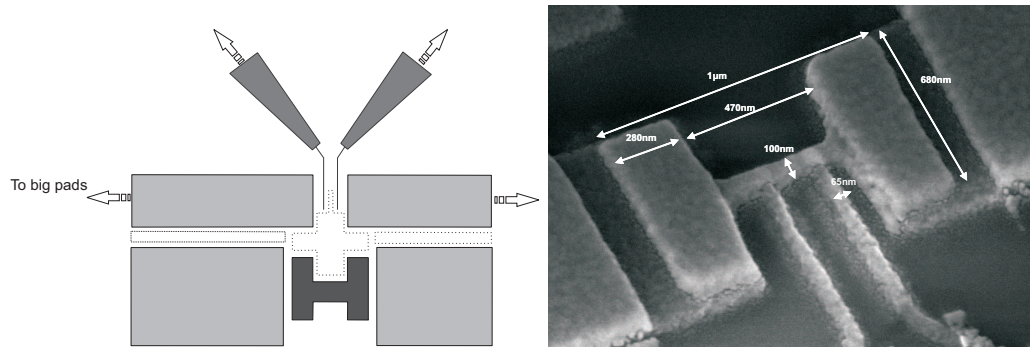
Figure 3.2: Example of a lithography CAD pattern and scanning electron micrograph of the result. Darker colors correspond to higher doses, dotted line is low, undercut dose. The sample shown is a Al-Cu SINIS test device.

cial in this system, and exceeding in either direction resulted in under-developed undercut or overdeveloped and fragile suspended masks.

E-beam patterning

Coated wafers were cut into small pieces of around 5 mm x 5 mm and patterned with a LEO Scanning Electronic Microscope (SEM) equipped with NPGS electron lithography system. The device outline was drawn on a CAD and the charge doses were set (see e.g., Fig. 3.2). The bilayer resist system requires a precise fine-tuning of doses and geometries for samples to be consistently repeatable. Care must be taken so that undercut is present only where it is strictly needed to maximize the stability of the suspended mask and prevent unwanted metallic "shadows" after lift-off. Large exposed areas and the high doses needed for small features, influence the patterning of the surrounding area by producing unwanted exposures. A large electric charge deposited on the insulating PMMA resist layer by the electron beam remains localized and tends to repel the other impinging electrons, causing broadening of the beam and unwanted exposures of the neighboring zones. This is called proximity effect and is one of the most relevant limiting factors for the resolution of e-beam lithography. To minimize this effect, a high acceleration voltage (30 kV) was used, but the proximity effect is never completely negligible. The sensitive co-polymer suffers especially from proximity effects making the pattern doses and the undercut doses strongly interdependent. However, with some pattern-dependent fine tuning, the bilayer shadow mask evaporation technique is able to offer great
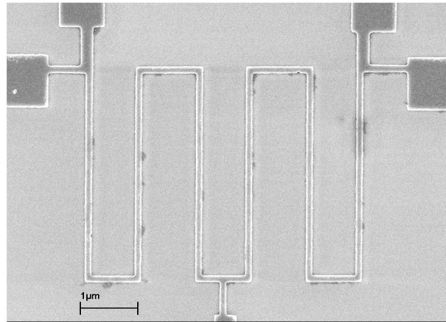
Figure 3.3: Scanning electron micrograph of a typical wire sample used to test resistivity of Ti and Cu metallic films.

flexibility for the realization of a wide range of devices.

E-beam evaporation

Once the samples were patterned and developed, they were transferred in the UHV chamber of our e-beam evaporator for metallic film deposition and fabrication of the tunneling junctions by natural oxidation in pure oxygen atmosphere.

Shadow-mask evaporation needs a highly directional deposition method, and e-beam evaporation provides the required anisotropy of the deposited film accretion. Metals are evaporated in UHV by focusing a thermoionically-generated electron beam on a refractory crucible containing the metal to be evaporated. The sample was placed on rotatable holder with two degrees of freedom, i.e. $360°$ rotation, $\pm 70°$ tilting. After the evaporation of the Al film, without breaking the vacuum, the sample was transferred to the load lock chamber for the oxidation process. The load lock chamber was thus filled with a given pressure of pure O_2 gas for a set amount of time. After the oxidation process is complete, the sample is re-transferred to the UHV chamber for the second angle evaporation creating the tunnel barriers where the two films overlap. Operating in UHV at pressures as low as some 10^{-11} Torr allows to deposit high-purity films, however the real bottleneck for metals purity is the electron beam focusing. We found out that even slightly improper alignment of the electron beam with the crucible implies evaporation of unwanted material from the neighboring areas, radically impairing purity of the more reactive materials. For superconducting metals, this reflects on a higher resistivity of the metallic film and lower critical temperature. Titanium is especially sensitive to this problem because of its gettering properties: a slight change in the electron gun alignment may trans-
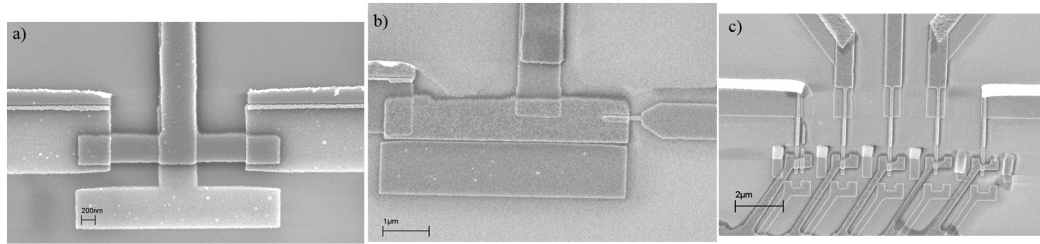
Figure 3.4: SEM images of devices that were fabricated for testing tunnel junctions of different size. Geometry (c) was developed to test several small barriers at a time. The irregular films that appear in bright white on the side leads and the top leads are residuals "shadows" that were left because of insufficient ultrasound cleaning, but do not interfere with the functionality of this particular device.

late into a rise of resistivity (at 4.2 K) from 0.3 to 10 μOhm·m. The resistivity of titanium films was measured performing four-contact measurements of test wires like the one shown in Fig. 3.3 immersed in liquid helium.

After the evaporation, the wafer was transferred to a 50°C acetone bath for liftoff. Mild ultrasound cleaning was necessary to remove residuals of shadow evaporation [see Fig. 3.4(c)]. Finally, the wafer piece with the device was mountend onto the sample holder and the contact pads were bonded to the holder leads. Samples were then transferred to the cryostat for measurements.

3.1.2 Tunnel barriers

The key step for the realization of a controllable Josephson junction by extraction of quasiparticles is the fabrication of tunnel barriers. With the development of the shadow-mask evaporation technique, it became possible to create reliable tunnel barriers with ease and versatility. An ideal tunnel barrier is formed by a thin insulating layer interposed between two metallic leads. The insulating layer should have a high dielectric constant and be defect-free, i.e. free from pinholes and any impurity that may interact with the tunneling electrons. For the simplicity of use and the good dielectric constant, aluminum oxide is used extensively as insulator in tunnel barriers [14]. An aluminum oxide layer can be grown onto an evaporated film of aluminum by natural oxidation, therefore eliminating the need of another deposition step. In most systems, a separate chamber is dedicated to the oxidation, performed either by injection of a set pressure of pure oxygen or in oxygen flow. In
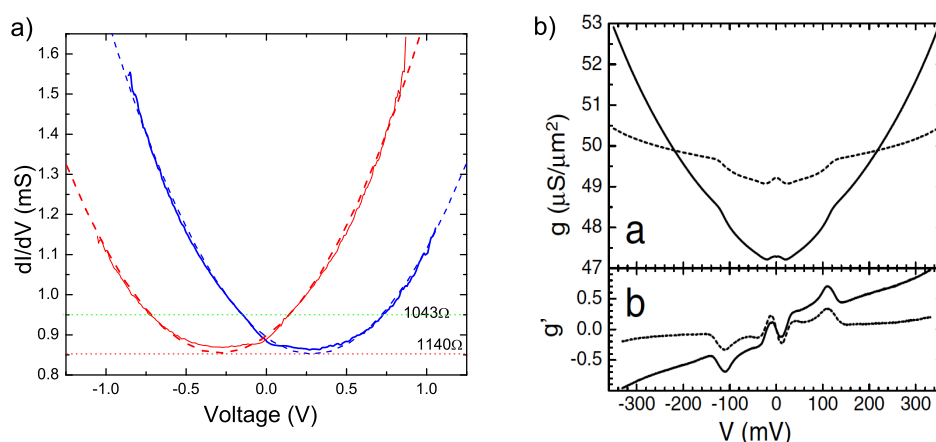
Figure 3.5: Panel (a): Differential conductance vs. voltage (solid line) and parabolic fit (dashed line) calculated from the current-voltage characteristic of a single Al-AlO$_x$-Cu tunnel junction. The red and blue data are measured by sweeping voltage in opposite direction, the green line shows conductance value at room temperature. Panel (b): Differential conductance vs. voltage from Al-AlO$_x$-Cu and Al-AlO$_x$-Au (dashed curve); the bottom plot shows conductance derivative. (b) adapted from [14]

our setup, the load lock chamber of the e-gun evaporator was used for the oxidation: the sample was loaded through this chamber and transferred to the UHV chamber ($10^{-10} \div 10^{-11}$ Torr was the typical base pressure), then the first aluminum layer was evaporated at the first angle (the pressure during evaporation was typically 10^{-8}) and re-transferred to the load lock without breaking the vacuum (the latter chamber was at $10^{-6} \div 10^{-7}$ Torr). The relevant parameter for the resistance of the resulting insulating barrier is oxidation time times pressure. We found out that a longer oxidation time at relatively low pressure produced more reliable barriers than quick oxidations at higher pressures. After this step, oxygen was pumped away and sample was re-transferred to the UHV chamber for the second angle evaporation and the formation of tunnel junctions.

Much time was devoted to the optimization of tunnel barriers. A large amount of data is available in the literature especially on Al-AlO$_x$-Cu systems, but barrier quality and specific resistance are strongly system-dependent, so that a thorough characterization was needed before implementation of the final devices. To assess the quality of a tunnel barrier some widely accepted criteria exist that do not need millikelvin temperatures. Barriers are usually described within the WKB approximation using the Simmons model [31] which gives a first order approximation for the
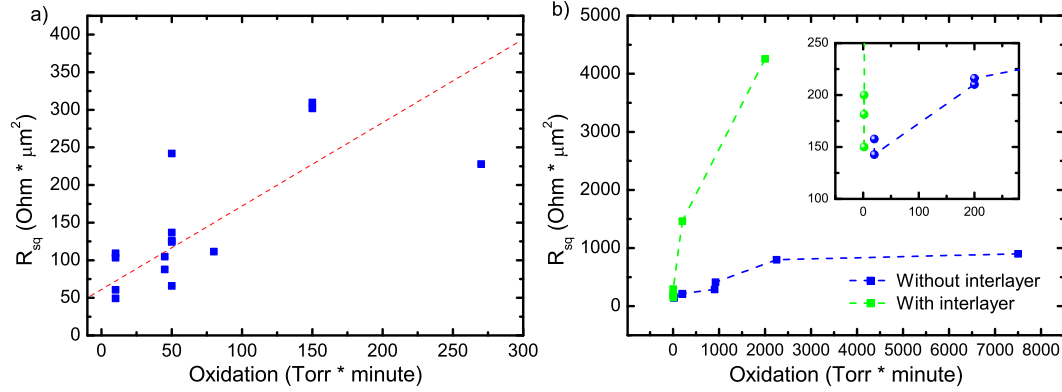
Figure 3.6: Panel (a): specific resistance versus oxidation time and pressure for a Al-Al$_x$O$_x$-Cu tunnel junction. The dashed linear dependence is reported as a guide for the eyes, as more data are in the lower specific resistance range which are in our interest. Panel (b): Comparison between Al-Al$_x$O$_x$-Ti junctions resistances (blue dataset) and Al-Al$_x$O$_x$-Al(5 nm)-Ti (green dataset) versus oxidation time and pressure. The latter system data are more similar to the Al-Al$_x$O$_x$-Cu system, proving that interdiffusion could be reduced.

junction conductance per area at low temperature

$$g(V) = g_0(1 + V^2/V_0^2) \qquad (3.1)$$

with $V_0 = \left(\frac{4\hbar^2}{e^2m}\right)\frac{\Phi_0}{s^2}$ and $g_0 = \frac{e^2\sqrt{2m\Phi_0}}{h^2 s}\exp\left(-\frac{2s}{\hbar}\sqrt{2m\Phi_0}\right)$, where s and Φ_0 represent barrier thickness and potential height respectively and m is the electron mass. For large enough voltage (V), the conductance is therefore expected to present parabolic behavior and this can be used as a preliminary check test. However, in Ref. [19], it was pointed out that a parabolic dependence is not sufficient to prove that electron tunneling is the main conduction mechanism. Differently, it is suggested to use the *increase* of zero-bias resistance of about 15% when going from room temperature to 4.2 K as a test to assess the quality of the junction. To test our samples we employed both criteria, making sure that we were producing barriers having about 15% increase of resistance from room temperature to 4.2 K and a parabolic behavior for the conductance. To test the reliability of the barriers we developed a number of different geometries (see Fig. 3.4), we started from the Al-AlO$_x$-Cu system to optimize the oxidation process, then moved to the Al-AlO$_x$-Ti system. Figure 3.5(a) shows the differential conductance vs. voltage from one of our Al-AlO$_x$-Cu barrier oxidized at 27 mTorr for 10', with junction area of 0.2 μm^2, and specific resistance $R_N \times \mathcal{A} = 228\ \Omega \cdot \mu$m^2. The current-voltage characteristic
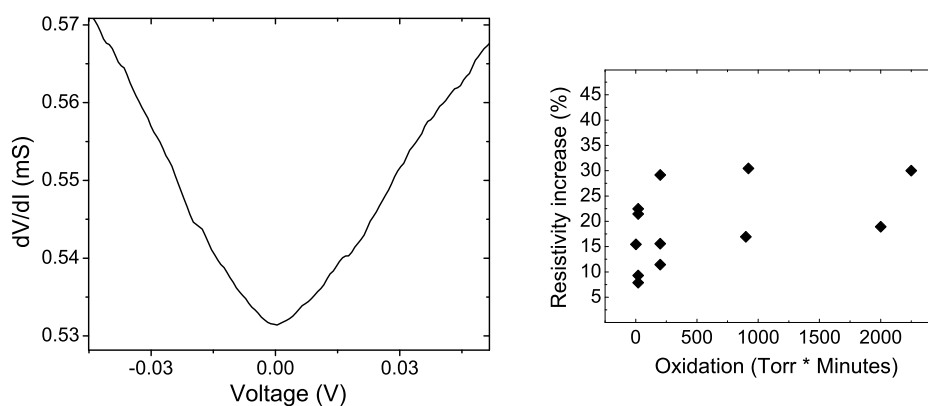
Figure 3.7: Panel (a): Differential conductance numerically calculated from a current voltage characteristic of two Al-Al$_x$O$_x$-Al(5 nm)-Ti in series, showing parabolic behavior. Panel (b): Increase in resistance cooling from room temperature to 4.2 K of different Al-Al$_x$O$_x$-Al(5 nm)-Ti junctions. An increase of at least 15% of resistance is an accepted indicator of the absence of defects in the barrier.

was obtained with a two-wire measurement and the conductance was numerically calculated by differentiation of the data. The two curves in Fig. 3.5 are measured by sweeping the voltage in opposite directions: this produces a displacement between them by two times the difference of the work function of aluminum (4.25 eV) and copper (4.4 eV). The sample shows an increase in resistance of about 11% from room temperature to 4.2K, as shown by the horizontal dotted lines. For a comparison, Fig. 3.5(b) shows the differential conductance of copper-aluminum and copper-gold tunnel junctions measured in Ref. [14].

The Al-AlO$_x$-Ti system was found to be more diffucult to exploit for the fabrication of tunnel barriers. The chemical reactivity of titanium causes part of the aluminum oxide of the barrier to diffuse into the bulk titanium [35], degrading both barrier quality and material purity. We demonstrated that it is nonetheless possible to obtain reliable tunnel barriers of low specific resistance with this system by over-oxidizing the aluminum layer [see blue dataset of Fig. 3.6(b)]. However, this happens only at the expense of the titanium purity, and we verified that in these junctions the titanium film had very low critical temperature or was not even superconducting at all. Al-Al$_x$O$_x$-Ti tunnel junctions, although feasible, are thus not suitable for our application. To solve this problem, we opted to introduce a 3 to 5 nm-thick aluminum interlayer between the aluminum oxide and the titanium. The green dataset in Fig. 3.6(b) shows a dataset of specific resistance for junctions

49
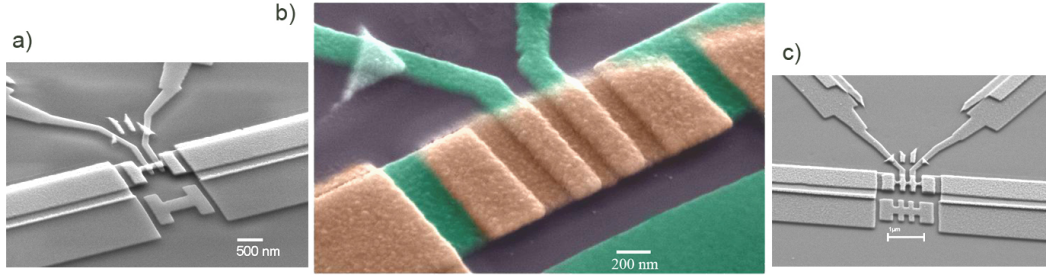
Figure 3.8: Scanning electron micrographs of two geometries explored for the S$_1$IS$_2$IS$_2$ device [(a) and (c)] and a typical sample of the final device [(b)]. The small inner junctions (probes) are used for measuring the Josephson current, the wider junctions (injectors) are used to control the quasiparticle distribution function in the titanium island through quasiparticle extraction.

with interlayer. The specific resistance is higher than a junction with the same oxidation parameters but without interlayer, suggesting that interdiffusion may be reduced. This is confirmed by the titanium critical temperature, which in junctions with interlayer varies between 200 and 300 mK. The aluminum interlayer critical temperature is strongly suppressed by proximity effect from the 45 nm-thick titanium film, and can be neglected in the final analysis. Figure 3.7 shows the results of the characterization of the final barriers, demonstrating the parabolic behavior of the conductance (left panel) and an increase in the resistance by more than 15% (right panel) when cooling the junction from room temperature to 4.2 K. The final device was thus fabricated with Al-Al$_x$O$_x$-Al(5nm)-Ti junctions.

3.2 S$_1$IS$_2$IS$_1$ controllable Josephson junctions

For the realization of the S$_1$IS$_2$IS$_2$ Al-Ti-Al device I tested a number of different geometries (see Fig. 3.8). The volume of the titanium island needs to be as small as possible to limit quasiparticle relaxation with phonons and allow the realization of an out of equilbrium distribution function. However, the tunnel barriers area needs to be wide enough to allow sufficient extraction rates, and this sets a limit for the island size. For this reason I tried to implement a dogbone-shaped profile for the titanium island [Fig. 3.8(a) and (c)] but I discovered that titanium wires 150 nm wide or less would not become superconducting. This sets an even higher limit to the titanium island size. The final geometry of the device is thus slightly bigger than the initial project [Fig. 3.8(b)], with a titanium island of (650 $\times$ 1500) nm^2.

The device was fabricated with the following processing steps. First a 40 nm aluminum film was evaporated a $0°$ at 3 Å/s, then it was oxidized at 20 mTorr for 20'. 5 nm of aluminum interlayer were evaporated at $51°$ followed by 40 nm of titanium at 16 Å/s at the same angle. The nominal purity of aluminum and titanium is 99.999%. The last evaporation step creates additional, electrically passive titanium islands that overlap the aluminum reservoirs (indicated as quasiparticle traps in Fig. 3.8) that provide better thermalization of the aluminum lateral electrodes.

After liftoff the device was glued (with Oxford heat-conducting varnish) to the copper sample holder of a dilution refrigerator which was in thermal contact with the mixing chamber. Big pads were bonded to the holder leads, and the sample was cooled down to the base temperature of the fridge for measurements.

Chapter 4

Experimental results and discussion

In this chapter I shall present the experimental results of the $S_1IS_2IS_1$ devices that I fabricated and measured, and the theoretical model we used to analyze them. The details of the processing are described in Chapter 3. A micrograph of one of the devices measured is shown in Fig. 4.1. The larger-gap superconductor is aluminum (green color) while the smaller-gap superconductor is titanium (brown color). The devices I shall present data from have the same geometry and fabrication parameters, detailed in the following. The titanium island is 40 nm thick and has a surface of (650 $\times$ 1500) nm^2, the aluminum reservoirs are 50 nm thick and (650 nm $\times$ 10 μm) each. The reservoirs are long to ensure good thermalization with the substrate, and passive titanium layers are overlapping over their length to provide better thermalization of the aluminum reservoirs [26]. The tunnel junctions were fabricated by oxidizing the aluminum layer at a pressure of 20 mTorr for 20'. Junction areas are 0.13 ± 0.01 μm^2 for probe junctions and 0.24 ± 0.02 μm^2 for injectors junctions, with a total specific resistance of about $\approx 150 - 170$ $\Omega \times \mu$m^2. The wider junctions are used to drive the island out of equilibrium by applying a voltage bias across them, while the smaller ones are used to measure the Josephson supercurrent.

Measurement technique

I performed all the low-temperature measurements in a dilution fridge with a base temperature of 35 mK. High frequency noise filtering was provided by 1.3 m of
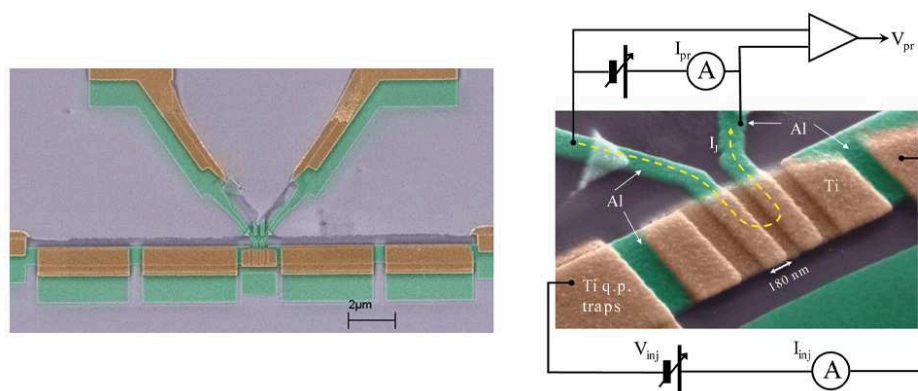
Figure 4.1: Colorized scanning electron micrograph of a typical sample. Green areas are aluminum, brown areas are titanium. The right panel shows a detailed view of the device with the setup used for measuring the Josephson junction versus injection.

Thermocoax cable at low temperature and by LC π-filters at room temperature. A variable DC voltage generator was used to provide floating voltage bias of injector junctions. Thermometry was done with a RuO_2 resistor calibrated against a Coulomb blockade thermometer [12]. The small probes were voltage biased by means of a function generator sweeping with very low frequencies (0.2 - 1 Hz) the voltage range of interest: above $\pm 2(\Delta_1 + \Delta_2)/e$ for full current-voltage characteristics or just the region around zero bias for Josephson current measurement. Voltage and current were pre-amplified and measured independently with a four-wire measurement for both the probing and injecting line. In the out-of-equilibrium measurements, injectors were biased from 0 to above $\pm 2(\Delta_1 + \Delta_2)/e$ while I-V characteristics of the probes were measured to monitor the behavior of the Josephson current. I performed all the low-temperature measurements at the Pico Laboratory, Helsinki University of Technology, under the supervision of Prof. J. P. Pekola and Dr. A. Savin.

4.1 Equilibrium data

As soon as the sample was cooled at low temperature, a preliminary analysis of its functionality was carried out by studying its properties at the equilibrium. The main electrical and physical characteristics of the sample (e.g., the normal-state resistance of the junctions and the critical temperature of the metallic films) are mea-
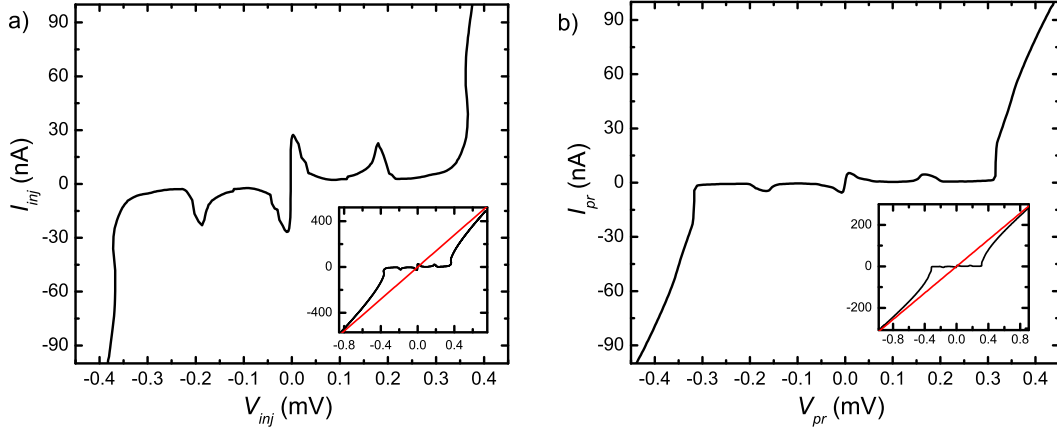
Figure 4.2: Current-voltage characteristics of sample I119C measured at 35 mK, shown on the same scales. The bottom right insets show the current behavior at large voltages, used to determine normal-state resistance (defined as the inverse of slope red line). Panel (a): I-V of injector junctions. Panel (b): I-V of probe junctions.

sured first. At this stage, we also assessed the quality of the junctions by measuring the increase in their normal-state resistance when cooling from room temperature to 4.2 K (see Sec. 3.1.2). Figure 4.2 shows the current-voltage characteristics measured for the series of the two injection junctions [Panel (a)] and probe junctions [Panel (b)]. The normal-state resistance is defined as the inverse of the slope of the line which the I-V asymptotically tends to [red line in the insets of Fig. 4.2]. The two samples which I shall present data from, will be labeled I119C and I119A, have normal-state resistances of 710 Ω (I119C) and 700 Ω (I119A) respectively for the injection junctions and 1.56 kΩ and 1.25 kΩ for the probe junctions. The resulting specific resistance is about 150-170 $\Omega \times \mu$m^2, with a 10% error due to the determination of junction area. The latter was obtained by inspecting the scanning electron micrographs of the devices.

From the current-voltage characteristics is possible to obtain an indication of the sum of superconducting gaps of aluminum and titanium, i.e., $(\Delta_1 + \Delta_2)$. This is done by measuring the voltage at which the onset of quasiparticle tunneling occurs, i.e., $V = 2(\Delta_1 + \Delta_2)/e$. In Fig. 4.2 we can see that the quasiparticle onset occurs at 365 μV for the injector junctions and at 340 μV for probe junctions. This discrepancy can be explained by assuming a different gap-smearing parameter γ in the density of states [see Eq. 1.9] for the junctions. This is a reasonable assumption, since γ phenomenologically takes into account any sub-gap conduction
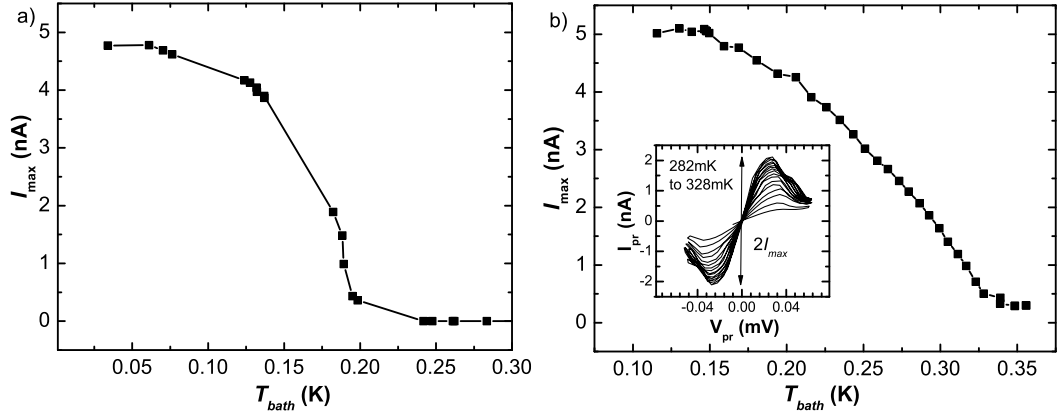
Figure 4.3: Maximum supercurrent at the equilibrium I_{max} versus bath temperature T_{bath} for Sample I119A (Panel a) and I119C (Panel b). The inset of Panel (b) shows the evolution of the zero-bias feature used to measure the maximum supercurrent at $T_{bath} = 282$ mK - 382 mK. Errors on voltage and current are within the instruments specification and below 1% so that no error bars are displayed.

channel. This includes impurities in the superconductors, but also pin-holes in the tunnel junctions which are more likely to be present in larger junctions like the injectors. A non-zero γ has also the effect of smearing the quasiparticle onset at $2(\Delta_1 + \Delta_2)/e$, as appears from Fig. 4.2, which displays a less abrupt quasiparticle current onset for the injector junctions [Panel (a)] than for the probes [Panel (b)]. From the current-voltage characteristics, we estimate $\gamma_{1,2} \approx 10^{-3} - 10^{-2}\Delta_{1,2}$, with a value slightly higher for the injectors junctions. From the temperature shift of the quasiparticle onset it would be possible to determine the energy gaps of both superconductors, but this rather high value of γ introduces an error on the determination of the value of $2(\Delta_1 + \Delta_2)/e$ which does not allow to clearly identify the two gaps. For the determination of the superconducting gap of titanium, we rather rely on the measurement of its critical temperature through the behavior of the supercurrent versus temperature at equilibrium. We identified the critical temperature of titanium as the temperature at which the supercurrent amplitude around zero voltage bias vanishes. Assuming that the BCS relation (1.3) holds for the gap values at equilibrium, from the titanium critical temperature T_{c2} we can find the zero-temperature value of superconducting gap $\Delta_2(0)$. We must keep in mind that interaction with the electromagnetic environment [17, 32], may cause the disappearance of the supercurrent at a lower temperature than the effective T_{c2} of titanium, so that its superconducting gap may be larger than the one actually estimated in this way.

55

Figure 4.3 displays the supercurrent I_{max} versus bath temperature T_{bath} that flows through the probe junctions at equilibrium for Sample I119C [Panel (a)] and I119A [Panel (b)]. The supercurrent manifests itself in the I-V as a peak of finite width around zero bias [see inset in Fig. 4.2(b)] rather than a sharp, infinite-slope feature. This is however expected for small Josephson junctions coupled with an electromagnetic environment [17]. We thus define as maximum observable Josephson current I_{max} half the sum of the amplitudes of the positive and negative peaks around zero bias. At low temperatures the supercurrent is saturated to its zero temperature value, ≈ 4.8 nA for I119C and ≈ 5 nA for I119A. This value is about one order of magnitude lower than the Ambegaokar-Baratoff (1.10) prediction of 64 nA. This is however expected for ultrasmall Josephson junctions [32].

At higher temperatures the supercurrent is gradually reduced, being completely suppressed at the critical temperature T_{c2} of the titanium layer ≈ 210 mK for Sample I119C and ≈ 340 mK for Sample I119A. Both samples were fabricated with the same processing parameters, but measured at different times. Sample I119C, which was measured later, shows a reduction of the critical temperature of titanium, which may indicate that aging can influence the purity of the material, possibly by inter-diffusion between the metallic and oxide layers [35].

4.2   Out-of-equilibrium data

Out-of-equilibrium measurements were obtained by applying a fixed voltage bias V_{inj} to the injector junctions and by measuring the corresponding I-V characteristic of the probe junctions. V_{inj} was then varied throughout the range of interest, i.e., $-2(\Delta_1 + \Delta_2)/e \lesssim V_{inj} \lesssim 2(\Delta_1 + \Delta_2)/e$. Figure 4.4(a) shows the zero bias feature used to determine I_{max} from the probes current-voltage characteristic for different values of injection voltage. Each curve and color correspond to a different value of V_{inj}, and were vertically offset for clarity. The supercurrent shows a non-monotonic behavior as a function of V_{inj}. As V_{inj} increases, the supercurrent is initially suppressed ($V_{inj} = 59$ μV), then it is partially regenerated with a smaller magnitude than that at equilibrium, and suppressed again ($V_{inj} = 109$ μV). The supercurrent is then maximized at $V_{inj} = 344$ μV and finally quenched for $V_{inj} = 400$ μV. Further increase of V_{inj} produces only heating of the central island and no supercurrent is observed. The full I_{max} versus V_{inj} dependence is shown on the left axis of Fig. 4.4(b). The right axis shows the I-V characteristics of the injector junctions at the same bath temperature. The plot shows the correspondence of the quasi-
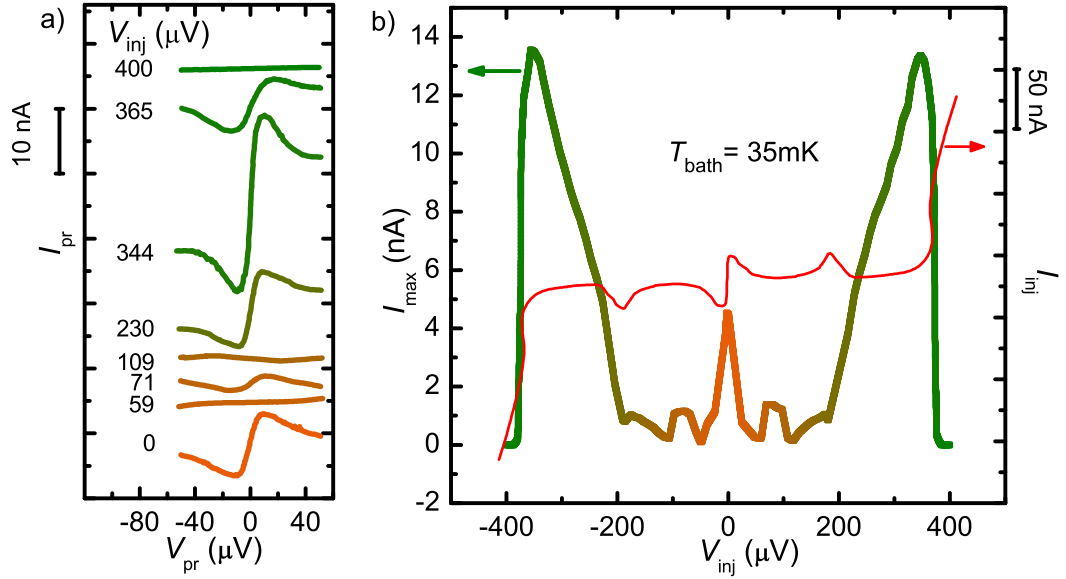
Figure 4.4: Panel (a): Current-voltage characteristics of the probe junctions at different bias voltages V_{inj} of injector junctions at $T_{bath} = 35$ mK for sample I119C. The curves are vertically offset for clarity. Each color corresponds to a different injection voltage $|V_{inj}|$. Largest enhancement happens at $|V_{inj}| \approx 340$ μV. Panel (b) shows the full dependance of I_{max} versus injectors bias voltage (thick line). The current behaves non-monotonically until it is fully suppressed at $|V_{inj}| \approx 400$ μm. The red line shows the I-V characteristics of injector junctions.

particle onset at $V_{inj} = 2(\Delta_1 + \Delta_2)/2$ with the final quenching of the supercurrent. The extra peaks in the middle of the positive and negative branch of the I-V are related to the supercurrent behavior at low voltage bias, as we shall show in the next section. Figure 4.5 shows the same set of measurements for Sample I119A. The sample was measured in a cryostat with a base temperature of 115 mK. This sample reproduces the same overall behavior of Sample I119C, and confirms the good reproducibility of the results.

Figure 4.6(a) displays the current-voltage characteristics of the probe junctions at $T_{bath} = 250$ mK $> T_{c2}$, showing the generation of the zero-bias peak at $V_{inj} = 350$ μV. Figure 4.6(b) shows I_{max} vs V_{inj} in the high temperature range (left axis) and the correspondent I_{inj} vs V_{inj} characteristic of injector junctions (right axis) for Sample I119C, and Fig. 4.6(c) shows the same injection data for Sample I119A. As temperature rises, I_{max} versus V_{inj} initially retain the same profile observed at low temperature, then as the critical temperature of titanium is approached, the equi-

57
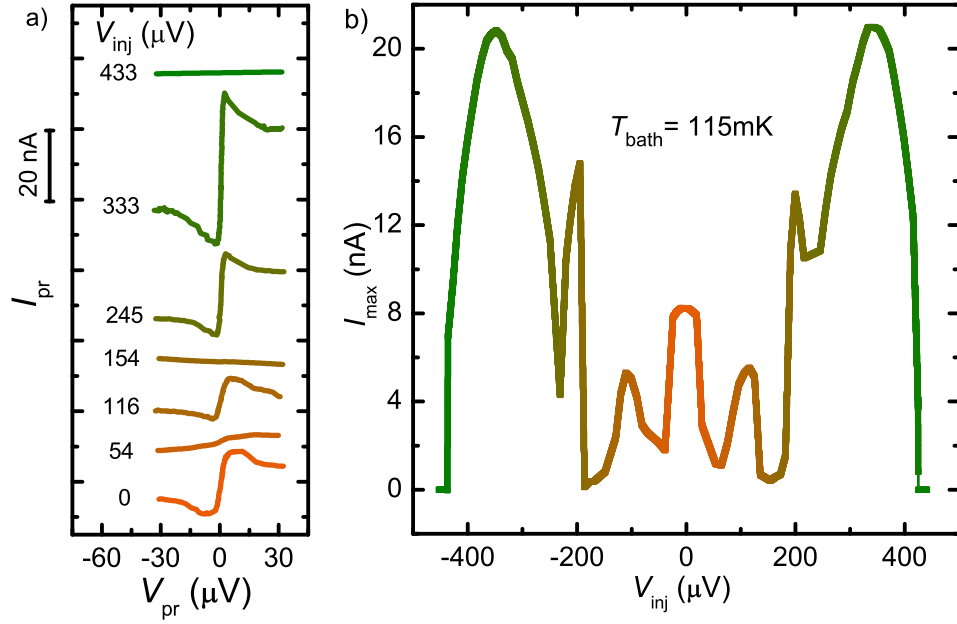
Figure 4.5: Panel (a): Current-voltage characteristics of probe junctions at different bias voltages V_{inj} of injector junctions at T_{bath}=115 mK for Sample I119A. The curves are vertically offset for clarity. Panel (b) shows the full dependance of I_{max} versus injectors bias voltage V_{inj}. Some secondary peaks are present, but the overall behavior is similar in both samples I119A and I119C.

librium supercurrent and the small peaks at low injection voltage vanish progressively. However, as temperature increase, the equilibrium supercurrent at $V_{inj} = 0$ vanishes sooner than the small peaks at low injection voltage [for instance see $T_{bath} = 190$ mK in Fig. 4.6(b) and $T_{bath} = 275$ mK, $T_{bath} = 325$ mK in Panel (c)]. These features are related to the titanium superconducting gap, so their behavior versus temperature indicates that some cooling mechanism is sustaining them at higher temperature. As we shall demonstrate in the next section, the junction is effectively cooling at the correspondent V_{inj}.

At even higher temperatures, when $T_{bath} > T_{c2}$ only the large supercurrent peak at $V_{inj} \approx 350$ μV survives. The behavior of the supercurrent above T_{c2} is displayed in Fig. 4.6(a). When $T_{bath} > T_{c2}$, titanium is initially in the normal state, and the equilibrium supercurrent is zero. By increasing V_{inj}, the titanium island is cooled into the superconducting state, and the supercurrent is generated almost up to the zero-temperature value. The supercurrent can be generated at temperatures much higher than T_{c2}. Figure 4.7 shows the supercurrent versus temperature behavior
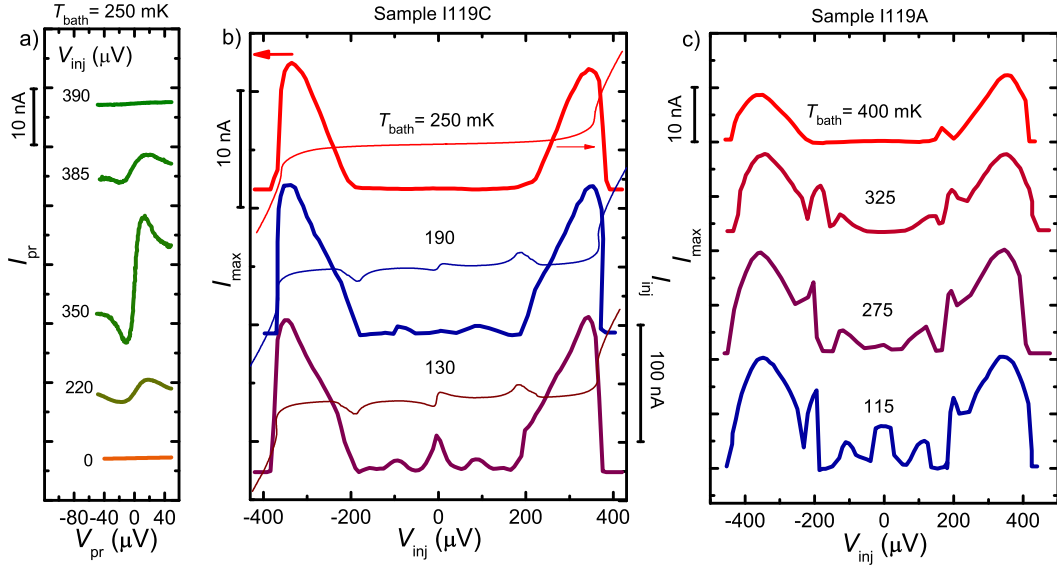
Figure 4.6: Supercurrent under injection at higher temperatures. Panel (a): Current-voltage characteristics of probe junctions at different bias voltages V_{inj} at $T_{bath} = 250$ mK for sample I119C. Above the critical temperature of titanium ($T_c = 210$ mK) the supercurrent is generated almost to its zero-temperature value. Panel (b) shows the full dependence of I_{max} versus injectors bias voltage at different bath temperatures (thick lines). Thin lines are the current-voltage characteristics of the injector junctions. Panel (c): Supercurrent versus injection for sample I119A. The highest temperature characteristic looks asymmetric because of a temperature dishomogeneity between the $V_{inj} > 0$ branch in which $T_{bath} \approx 350$ mK and $V_{inj} < 0$ branch in which $T_{bath} \approx 400$ mK.

at equilibrium and for some chosen values of V_{inj}. V_{opt} is the injection voltage that maximizes the supercurrent, which is slightly different in the two samples due to the different critical temperature values of the titanium layer. Also, the supercurrent at injection voltage $V_{inj} = 325$ μm for Sample I119C is shown in Fig. 4.7(a). This curve shows clearly the saturation of I_{max} at low temperature under injection. The data at V_{opt} show that for both sample is possible to generate a supercurrent above the critical temperature of titanium, up to about $1.6\,T_{c2}$. This means that there is a rather wide temperature range where we can cool the titanium island from the normal state down into the superconducting state by hot quasiparticle extraction.

4.3 Discussion

In order to analyze the data we have assumed that the titanium island is in the hot electron regime: electron-electron scattering drives the electronic system in S_2 into
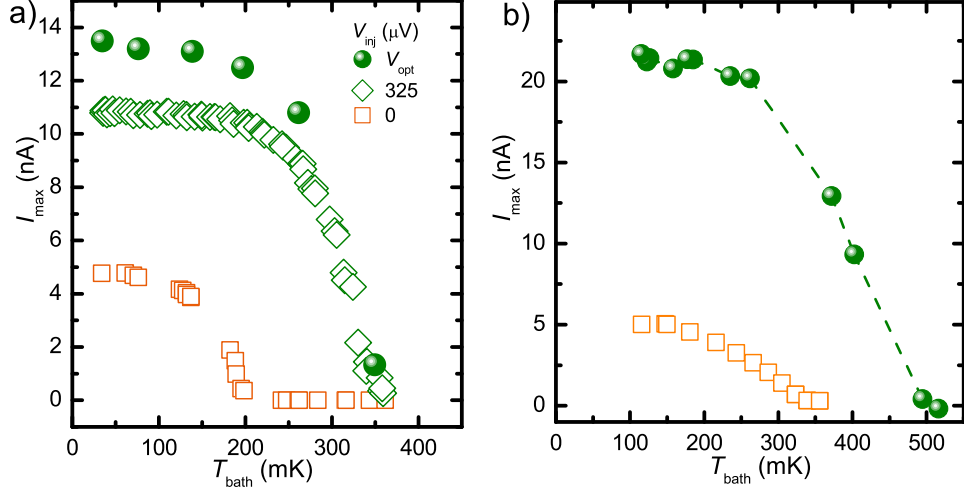
Figure 4.7: Supercurrent versus temperature at the equilibrium and for different injection values. Panel (a): Data for Sample I119C. Panel (b): Data for Sample I119A. V_{opt} is the injection voltage at which supercurrent is maximized. Supercurrent can be generated well above the critical temperature of titanium in both samples. All the curves show saturation of the supercurrent at low temperatures.

a local thermal (quasi)equilibrium described by the Fermi-Dirac distribution (1.11). The quasiparticle distribution is thus characterized by an electronic temperature T_e different from that of the phonon lattice T_{ph}. Data from the $S_1IS_2IS_1$ measurement have thus been analyzed with the quasiequilibrium model, as outlined in Sec. 1.3.2. This model uses the heat balance equation (1.22) to find the electronic temperature of S_2 for each injection voltage, and the generalized Ambegaokar-Baratoff expression (1.18) to calculate the supercurrent versus injection voltage. In Fig. 1.11(b) we showed a theoretical prediction for the supercurrent versus injection voltage in a $S_1IS_2IS_1$ structure with gap ratio Δ_2/Δ_1=0.3 and $\gamma_{1,2} = 10^{-4}\Delta_{1,2}$ to take into account for sub-gap conduction in the density of states of each superconductor [see Eq. 1.9]. A calculation with these parameters does not reproduce the non-monotonic behavior of the Josephson current versus injection experimentally observed [see Fig. 4.4], namely, no suppression is present at low injection voltages. However, this suppression is successfully reproduced as soon as we introduce a sufficiently large γ parameter in the density of states. Figure 4.8(a) shows the calculated supercurrent versus injection with parameters similar to those of our device: $T_{c,1} = 1.0$ K, $T_{c,2} = 180$ mK, $\gamma_2 = 10^{-2}\Delta_2$ and normal-state resistance of probe
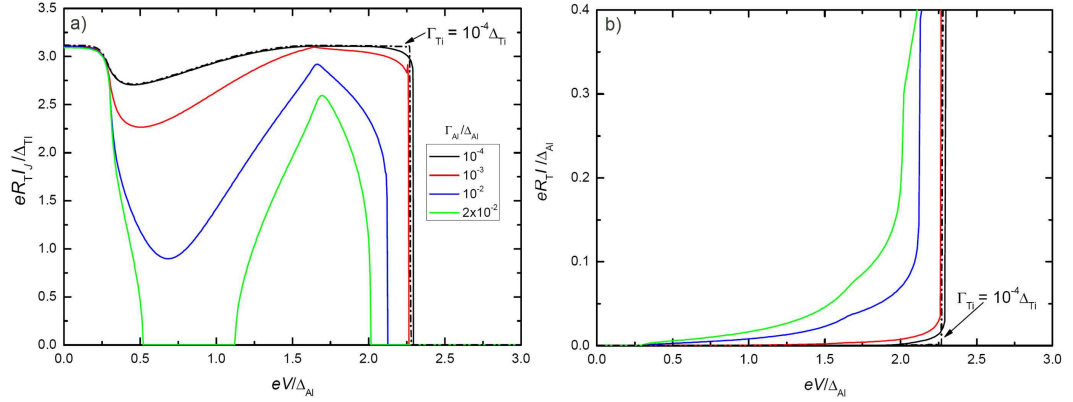
Figure 4.8: Panel (a): Calculated critical current versus injection for a $S_1IS_2IS_1$ junction in the quasiequilibrium regime for different values of depairing parameter γ_1 [indicated as Γ_{Al}]. The other essential parameters are: $T_{c1} = 1.0$ K, $T_{c2} = 180$ mK, $\gamma_2 = 10^{-2}\Delta_2$, and normal-state resistance of probe junctions $R_J = 1$ kΩ. Panel (b): Quasiparticle current-voltage characteristics of a $S_1IS_2IS_1$ device with the same parameters.

junctions $R_N = 1$ kΩ. The calculation is performed for $T_{bath} = 35$ mK and with different values of γ_1 (shown in the inset), the dash-dotted black curve is calculated with $\gamma_{1,2} = 10^{-4}\Delta_{1,2}$. The simulation shows that for $\gamma = 2 \cdot 10^{-2}\Delta_1$ the supercurrent is completely suppressed for low injection voltages, matching the behavior observed in our experiment. Figure 4.8(b) shows the quasiparticle current-voltage characteristics of the probe junctions with the same parameters as in Panel (a). The onset of the quasiparticle conduction is smeared by increasing $\gamma_{1,2}$ but notably the I-V's do not show the extra features present at $V \approx (\Delta_1 + \Delta_2)/e \approx 180$ μV in Fig. 4.2, instead they show a nearly monotonic dependence of current versus voltage.

The extra features in the I-V are connected to the generation of the small peaks in the critical current versus injection at low injection voltage, shown in Fig. 4.4. Their existence can be explained qualitatively within a simple model. The key observation is that the bias-devoltage dependence of the current in a single injector junction is non-monotonic because it can be carried both by Cooper pairs (supercurrent around zero voltage) and by quasiparticle (near and above gap voltage). Then, as a function of the bias voltage V_{inj} across the two injection junctions, the evolution of the voltage across each individual junction is as follows. Around zero bias, both junctions carry supercurrent, therefore the voltage drop across both of them is zero [see Fig. 4.9(a)]. For the left (L) and right (R) junction, we can thus write $V_L = V_R = 0$. As V_{inj} increases, one of the junctions, i.e. the one with smaller critical current, switches into the quasiparticle branch. The voltage drop across this "weaker" junction [e.g., the left one (L)] is then equal to the total voltage
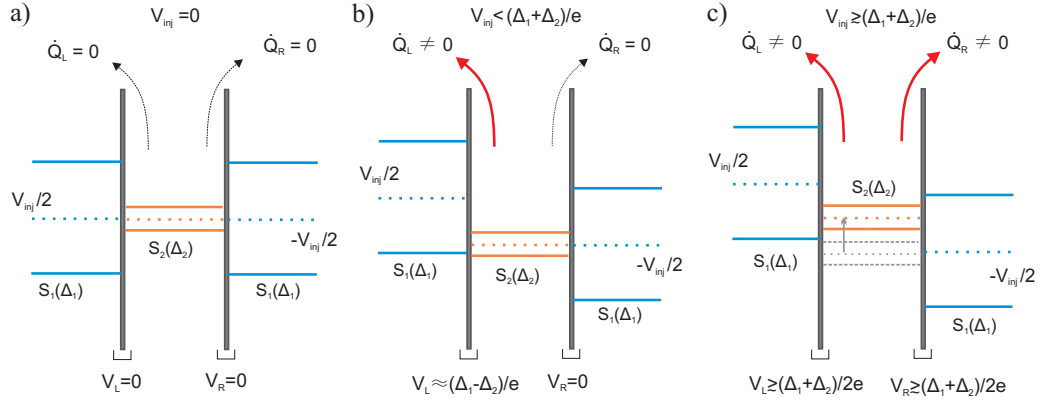
Figure 4.9: Schematic band diagram of a $S_1IS_2IS_1$ junction at different injection regimes. Subscript L and R indicates left and right junction, respectively. $\dot{Q}$ is the heat extracted from each junction. Panel (a): $V_{inj} \approx 0$, both junctions carry electrical current by Cooper pair tunneling, the voltage drop is zero on both. Panel (b): Below $V_{inj} \approx (\Delta_1 + \Delta_2)/e$ one of the two junction carries current by quasiparticle (e.g., the left one as in the scheme) while the other carries current by Cooper pair tunneling. The potential of the central island adjusts accordingly. Panel (c): As $V_{inj} \gtrsim (\Delta_1 + \Delta_2)/e$, also the other junction switches to quasiparticle branch and the voltage drop across them is symmetrical. The grey outline shows the central island in the asymmetric configuration, before the switch.

V_{inj}, so that we have: $V_L = V_{inj}$ and $V_R = 0$. This is the situation depicted in Fig. 4.9(b): the switching to the quasiparticle branch can be represented as the central island potential "adjusting" so that its Cooper-pair energy level and that of one of the reservoirs remain matched, while the other reservoir carries current by quasiparticle tunneling. As soon as one of the junctions starts conducting by quasiparticle tunneling, the heat extracted is different than zero ($\dot{Q}_L \neq 0$), reaching maximum cooling power at $V_{inj} \approx \Delta_1 - \Delta_2/e$, as expected for a single S_1IS_2 junction (see Sec. 1.3.2). Because of this cooling effect, the Josephson critical current of the probe junctions increases, and this corresponds to the peak at low injection voltage in the I_{max} vs. V_{inj} characteristics. Above this voltage, as $V_{inj} = (\Delta_1 + \Delta_2)/e$ one of the two junctions reaches the steep onset of quasiparticle current: this corresponds to the right edge of the peak in the middle of the I_{inj} vs. V_{inj} characteristics [see Fig. 4.2(a)]. Above this bias, also the second junction [i.e., the right (R) injector, as in Fig. 4.9(c)] switches into quasiparticle branch, providing finite cooling power, i.e., $\dot{Q}_R \neq 0$. Now the voltage is divided approximately equally across the two junctions, and at voltages above $(\Delta_1 + \Delta_2)/e$ the cooling power increases pro-
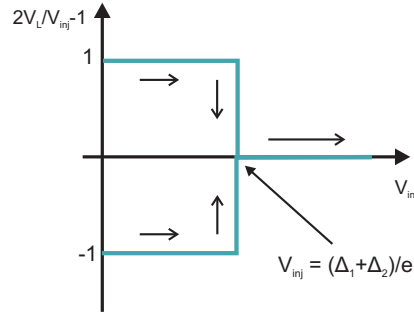
Figure 4.10: Plot of the quantity $2V_L/V_{inj} - 1$ representing the behavior of the potential across one of the injector junctions (i.e., the L junction).

gressively until it maximizes at $2(\Delta_1 - \Delta_2)/e$ [see Sec. 1.3.2]. Here both junctions are at their maximum cooling power, and this corresponds to the larger maximum in the probe supercurrent versus injection [see Fig. 4.4(b)]. The final increase of current I_{inj} in the injector junctions occurs at $2(\Delta_1 + \Delta_2)/e$, where both junctions have an approximately equal voltage corresponding to the sharp onset of quasiparticle current. This implies heating of the S_2 island, and subsequent quenching of the probe supercurrent.

A more quantitative analysis can be carried out as follows. The total electric current flowing through left and right injector can be written as the sum of the Josephson and the quasiparticle currents, i.e., $I_{inj}^{L,R} = I_J^{L,R} + I_{qp}^{L,R}$, where $I_J^{L,R} \neq 0$ for $V_{L,R} = 0$ is the Ambegaokar-Baratoff supercurrent (1.18), and $I_{qp}^{L,R}$ is the quasiparticle current given by

$$I_{qp}^{L,R}(V_{inj}) = \pm \frac{1}{R_T} \int_{-\infty}^{\infty} D_1(\tilde{\epsilon}_{L,R}) D_2(\bar{\epsilon})[f_0(\tilde{\epsilon}_{L,R}, T_{bath}) - f(\bar{\epsilon}, T_e)]d\epsilon. \qquad (4.1)$$

Here $\tilde{\epsilon}_{L,R} = \epsilon \mp eV_{inj}/2$, $\bar{\epsilon} = \epsilon - e(V_{inj}/2 - V_L)$, $R_T = 710\ \Omega$ is the injectors normal-state resistance, and we have assumed $\gamma_{1,2} = 5 \cdot 10^{-3}\Delta_{1,2}$ in the density of states $D_{1,2}$ (see Eq. 1.9), that depends also on $\Delta_1(T_{bath})$ and $\Delta_2(T_e)$. The superconducting gaps are calculated from T_{bath} and T_e assuming a BCS dependence of the gaps (1.2). At zero temperature we have $\Delta_{1,2}(0) = 1.764\,k_B T_{c1,c2}$, that with $T_{c1} = 1.2$ K and $T_{c2} = 210$ mK, gives $\Delta_1 = 32\ \mu$V and $\Delta_2 = 182\ \mu$V. The voltage drop V_L (V_R) across each junction follows from the conservation of the total current, $I_{inj}^L = I_{inj}^R$ with the constraint that $V_L + V_R = V_{inj}$. The solution for V_L is

$$\begin{aligned} \frac{2V_L}{V_{inj}} - 1 &= \pm 1 \quad \text{for} \quad 0 < V_{inj} \leq (\Delta_1 + \Delta_2)/e \\ V_L &= V_{inj}/2 \quad \text{for} \quad V_{inj} > (\Delta_1 + \Delta_2)/e. \end{aligned} \qquad (4.2)$$

63

The solution is graphically represented in Fig. 4.10. The plus or minus sign in the first case indicates that only one junction switches to quasiparticle branch as soon as V_{inj} becomes larger than zero. If the left junction switches to the quasiparticle regime, then $V_L = V_{inj}$ and $V_R = 0$ and in (4.1) $\bar{\epsilon} = \epsilon + eV_{inj}/2$. If the right one does, we have $V_L = 0$, $V_R = V_{inj}$ and $\bar{\epsilon} = \epsilon - eV_{inj}/2$. With the symmetric solution we have instead $\bar{\epsilon} = \epsilon$, i.e., the potential of the central island S_2 does not shift up or down.

With the same definitions, we can find the heat current flowing to and from the S_2 island $\dot{Q}_{L,R}$

$$\dot{Q}_{L,R}(V_{inj}) = \pm\frac{1}{e^2 R_T} \int_{-\infty}^{\infty} D_1(\tilde{\epsilon}_{L,R}) D_2(\bar{\epsilon})[f_0(\tilde{\epsilon}_{L,R}, T_{bath}) - f(\bar{\epsilon}, T_e)]\bar{\epsilon} d\epsilon. \qquad (4.3)$$

The electronic temperature in the S_2 island can be found from the energy-balance equation

$$\dot{Q}_L(V_{inj}, T_{bath}, T_e) + \dot{Q}_R(V_{inj}, T_{bath}, T_e) = 0, \qquad (4.4)$$

where we have neglected the electron-phonon interaction contribution (that would lead only to minor corrections). Note that the expression of the heat flow through the junction (4.3) depends on the density of states D_2 which is a function of $\Delta_2(T_e)$, therefore the equations must be solved self-consistently.

Once T_e is known, the maximum Josephson current of the probes junction is found through the generalized Ambegaokar-Baratoff equation (1.18), which becomes

$$I_J = -\frac{1}{2eR_J} \left| \int_{-\infty}^{\infty} dE \left\{ \mathbf{f}_2 \cdot \mathrm{Re}\mathcal{F}_2(E) \cdot \mathrm{Im}\mathcal{F}_1(E) + \mathbf{f}_1 \cdot \mathrm{Re}\mathcal{F}_1(E) \cdot \mathrm{Im}\mathcal{F}_2(E) \right\} \right|,$$

where $\mathbf{f}_{1,2} = [1 - 2f_0(E, T_{bath,e})]$, $\mathcal{F}_{1,2}(E) = \Delta_{1,2}/\sqrt{(E + i\gamma_{1,2})^2 - \Delta_{1,2}^2}$ and $R_J = 1.56$ kΩ is the probe junctions normal-state resistance. T_{bath} is the temperature of S_1, which is assumed to be in equilibrium. The results of these calculations are shown in Fig. 4.11. The current-voltage characteristics of the injector junctions are displayed on the right axis of Fig. 4.11(a) for different bath temperatures. The Josephson current in the injection junction is present as long as $T_{bath} < T_{c2}$, and in addition, the I_{inj} vs V_{inj} characteristic shows a peak centered in the middle of the characteristics similar to what is observed in the experiment (see Figs. 4.2, 4.4, 4.6). The probes critical current versus injection characteristics are displayed on the left axis of Fig. 4.11(a) for the same bath temperatures. The data on the maximum supercurrent presented in Figs. 4.4, 4.6 resemble those of the model
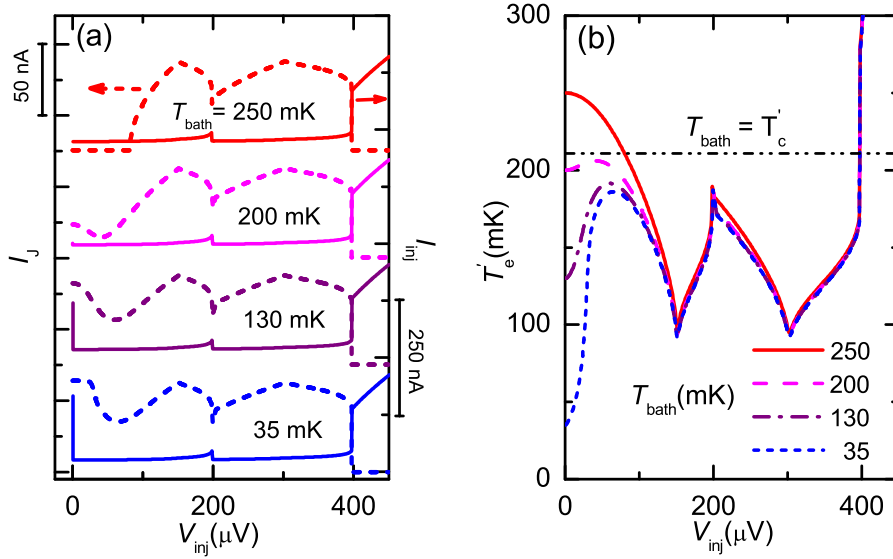
Figure 4.11: Panel(a): Critical current I_J versus V_{inj} calculated for a few values of T_{bath} (left axis, dashed line). I_{inj} versus V_{inj} calculated at the same T_{bath} (right axis, full line). The calculation is performed with essential parameters of Sample I119C: injectors normal-state resistance $R_T = 710\ \Omega$, probes $R_J = 1.56\ \text{k}\Omega$, $T_{c2} = 210$ mK, $T_{c1} = 1.2$ K, $\gamma_{1,2} = 5 \cdot 10^{-3} \Delta_{1,2}$. Panel (b): Electronic temperature T_e of the S_2 island for the same bath temperatures. The horizontal dash-dotted line represents its critical temperature.

apart from details that we attribute to an oversimplified thermal model.

Figure 4.11(b) shows the electronic temperature T_e calculated from Eq. 4.4 at the corresponding bath temperatures. For $T_{bath} \leq 200$ mK the electron gas is initially heated, inducing supercurrent suppression in the same voltage range. This heating is caused by the assumpion of a finite sub-gap conductance [12]. Increasing V_{inj} leads to the cooling-heating-cooling behavior that produces the two peaks in the supercurrent, and finally, for large V_{inj}, T_e is increased until the critical temperature of S_2 is exceeded.

In the high temperature regime, i.e., $T_{bath} = 250$ mK, the electron system starts being cooled as soon as $V_{inj} > 0$, and T_e drops below the critical temperature driving S_2 into the superconducting state. Then the plot follows the same behavior as at lower bath temperatures.

Albeit not quantitatively fully accurate, this simple thermal model is thus able to describe the main features of the experimental data of supercurrent versus injection, and explains the extra features in the current-voltage characteristics that had previously been identified in the literature [23], but lacked a physical interpretation.

Conclusions

The main results of this thesis work are a successful demonstration of all-superconducting Josephson junctions controlled by extraction of quasiparticles, and the first direct observation of the behavior of the Josephson supercurrent in an out-of-equilibrium superconductor. By inducing an out-of-equilibrium distribution function by quasiparticle extraction from a superconducting control line I was able to demonstrate heating and cooling of a mesoscopic titanium island. This allowed the observation of the supercurrent at lattice temperatures up to almost twice the critical temperature of titanium, thus demonstrating an electron-cooling effect capable of driving the metal from the normal state into the superconducting one at bath temperatures around 350-400 mK. This phenomenology was consistently reproduced in all measured devices.

About the processing steps, some useful results on the behavior of aluminum oxide for the case of interfaces with chemically active superconducting metals like titanium deserve mention. Refinements in the shadow-evaporation technique allowed to reproducibly fabricate aluminum-titanium tunnel junctions with a good flexibility in terms of specific resistance and geometry. Protocols were optimized to consistently fabricate superconducting Al-Al$_x$O$_x$-Ti junctions with specific resistance down to 100 Ohm·μm^2, and sizes smaller than 150 μm x 150 μm. This knowledge will be very useful for the development of other devices to further explore out-of-equilibrium behavior with different materials and geometries.

Our analysis of the S$_1$IS$_2$IS$_1$ junctions led to the observation of new charge transport phenomena in superconductive tunnel junctions. In particular, we demonstrated that the presence of two different mechanisms of charge transport in superconductors produces peculiar effects in multiple superconducting junctions. The accepted quasiequilibrium model was modified to include these new features. This model was then able to reproduce satisfactorily from a qualitative point of view the data of the measured samples.

Although a qualitative interpretation of the data was presented, some additional features of the supercurrent behavior deserve further investigation. A non-equilibrium theory modified to implement the non-monotonic behavior of the current versus voltage in superconducting junction is probably needed to explain some instabilities observed at the edges of the major features in the data.

The demonstrated electron cooling effect opens the way for a number of new developments. For instance, a low critical temperature superconductor like titanium may be exploited as the last section of a multi-stage solid-state refrigerator with very low base temperatures. For this purpose, similar structures may be explored by using different, higher critical temperature superconductors.

Bibliography

[1] V. Ambegaokar and A. Baratoff, *Tunneling between superconductors*, Physical Review Letters **10** (1963), 486–489.

[2] J. J. A. Baselmans, A. F. Morpurgo, B. J. van Wees, and T. M. Klapwijk, *Reversing the direction of the supercurrent in a controllable Josephson junction*, Nature **397** (1999), 43–45.

[3] J. J. A. Baselmans, A. F. Morpurgo, B. J. van Wees, and T. M. Klapwijk, *Tunable supercurrent in superconductor/normal metal/superconductor josephson junctions*, Superlattices and Microstructures **25** (1999), 973–982.

[4] J. J. A. Baselmans, B. J. van Wees, and T. M. Klapwijk, *Nonequilibrium supercurrent transport in controllable superconductor-normal metal-superconductor junctions*, Physical Review B **63** (2001), 094504.

[5] M. G. Blamire, E. C. G. Kirk, J. E. Evetts, and T. M. Klapwijk, *Extreme critical-temperature enhancement of al by tunneling in $Nb/AlO_x/Al/AlO_x/Nb$ tunnel junctions*, Physical Review Letters **66** (1991), 220–223.

[6] C. C. Chi and J. Clarke, *Enhancement of the energy gap in superconducting aluminum by tunneling extraction of quasiparticles*, Physical Review B **20** (1979), 4465–4473.

[7] A. M. Clark, N. A. Miller, A. Williams, S. T. Ruggiero, G. C. Hilton, L. R. Vale, J. A. Beall, K. D. Irwin, and J. N. Ullom, *Cooling of bulk material by electron-tunneling refrigerators*, Applied Physics Letters **86** (2005), 173508.

[8] R. C. Dynes, J. P. Garno, G. B. Hertel, and T. P. Orlando, *Tunneling study of superconductivity near the metal-insulator transition*, Physical Review Letters **53** (1984), 2437–2440.

[9] B. Frank and W. Krech, *Electronic cooling in superconducting tunnel junctions*, Physics Letters A **235** (1997), no. 3, 281–284.

[10] P. G. De Gennes, *Superconductivity of metals and alloys*, W.A. Benjamin Inc., 1966.

[11] F. Giazotto, T. T. Heikkilä, F. Taddei, R. Fazio, J. P. Pekola, and F. Beltram, *Mesoscopic supercurrent transistor controlled by nonequilibrium cooling*, Journal of Low Temperature Physics **136**, 435–452.

[12] F. Giazotto, T. T. Heikkila, A. Luukanen, A. M. Savin, and J. P. Pekola, *Opportunities for mesoscopics in thermometry and refrigeration: Physics and applications*, Reviews of Modern Physics **78** (2006), 217.

[13] F. Giazotto and J.P. Pekola, *Josephson tunnel junction controlled by quasiparticle injection*, Journal of Applied Physics **97** (2005), 023908.

[14] K. Gloos, P. J. Koppinen, and J. P. Pekola, *Properties of native ultrathin aluminium oxide tunnel barriers*, Journal of Physics Condensed Matter **15** (2003), 1733–1746.

[15] R. E. Harris, *Cosine and other terms in the josephson tunneling current*, Physical Review B **10** (1974), 84–94.

[16] D. R. Heslinga and T. M. Klapwijk, *Enhancement of superconductivity far above the critical temperature in double-barrier tunnel junctions*, Physical Review B **47** (1993), 5157–5164.

[17] G. L. Ingold, H. Grabert, and U. Eberhardt, *Cooper-pair current through ultrasmall josephson junctions*, Physical Review B **50** (1994), 395–402.

[18] J. Jochum, C. Mears, S. Golwala, B. Sadoulet, J. P. Castle, M. F. Cunningham, O. B. Drury, M. Frank, S. E. Labov, F. P. Lipschultz, H. Netel, and B. Neuhauser, *Modeling the power flow in normal conductor-insulator-superconductor junctions*, Journal of Applied Physics **83** (1998), 3217–3224.

[19] B. J. Jonsson Akerman, R. Escudero, C. Leighton, S. Kim, I. K. Schuller, and Rabson, *Reliability of normal-state current-voltage characteristics as an indicator of tunnel-junction barrier quality*, Applied Physics Letters **77** (2000), 1870.

[20] M. A. Laakso, P. Virtanen, F. Giazotto, and T. T. Heikkilä, *Nonequilibrium characteristics in all-superconducting tunnel structures*, Physical Review B **75** (2007), 094507.

[21] M. M. Leivo, J. P. Pekola, and D. V. Averin, *Efficient peltier refrigeration by a pair of normal metal/insulator/superconductor junctions*, Applied Physics Letters **68** (1996), 1996–1998.

[22] A. Luukanen, M. M. Leivo, J. K. Suoknuuti, A. J. Manninen, and J. P. Pekola, *On-chip refrigeration by evaporation of hot electrons at sub-kelvin temperatures*, Journal of Low Temperature Physics **120**, 281–290.

[23] A. J. Manninen, J. K. Suoknuuti, M. M. Leivo, and J. P. Pekola, *Cooling of a superconductor by quasiparticle tunneling*, Applied Physics Letters **74** (1999), 3020–3022.

[24] A.F. Morpurgo, T.M. Klapwijk, and T.M. Van Wees, *Hot electron tunable supercurrent*, Applied Physics Letters **72** (1998), 966–968.

[25] I. P. Nevirkovets, *Modification of current-voltage characteristics of double-barrier tunnel junctions under the influence of quasiparticle extraction*, Physical Review B **56** (1997), 832–837.

[26] J. P. Pekola, D. V. Anghel, T. I. Suppula, J. K. Suoknuuti, A. J. Manninen, and M. Manninen, *Trapping of quasiparticles of a nonequilibrium superconductor*, Applied Physics Letters **76** (2000), 2782–2784.

[27] J. P. Pekola, T. T. Heikkilä, A. M. Savin, J. T. Flyktman, F. Giazotto, and F. W. J. Hekking, *Limitations in cooling electrons using normal-metal-superconductor tunnel junctions*, Physical Review Letters **92** (2004), 056804.

[28] S. Rajauria, P. S. Luo, T. Fournier, F. W. J. Hekking, H. Courtois, and B. Pannetier, *Electron and phonon cooling in a superconductor–normal-metal–superconductor tunnel junction*, Physical Review Letters **99** (2007), 047004.

[29] A. M. Savin, J. P. Pekola, J. T. Flyktman, A. Anthore, and F. Giazotto, *Cold electron josephson transistor*, Applied Physics Letters **84** (2004), 4179–4181.

[30] D. R. Schmidt, R. J. Schoelkopf, and A. N. Cleland, *Photon-mediated thermal relaxation of electrons in nanostructures*, Physical Review Letters **93** (2004), 045901.

[31] J. G. Simmons, *Generalized formula for the electric tunnel effect between similar electrodes separated by a thin insulating film*, Journal of Applied Physics **34** (1963), 1793–1803.

[32] A. Steinbach, P. Joyez, A. Cottet, D. Esteve, M. H. Devoret, M. E. Huber, and John M. Martinis, *Direct measurement of the josephson supercurrent in an ultrasmall josephson junction*, Physical Review Letters **87** (2001), 137003.

[33] M. Tinkham, *Introduction to superconductivity*, third ed., McGraw-Hill, 1996.

[34] F. C. Wellstood, C. Urbina, and John Clarke, *Hot-electron effects in metals*, Physical Review B **49** (1994), 5942–5955.

[35] A. Zalar, M. Baretzky, S. Hofmann, M. Ruhle, and P. Panjan, *Interfacial reactions in Al_2O_2/Ti, Al_2O_3/Ti_3Al and $Al_2O_3/TiAl$ bilayers*, Thin Solid Films **352** (1999), 151–155.

Acknowledgements